Resonating-group study of baryon-baryon interactions for the complete baryon octet: NN interaction

AUTHOR(S):

Fujiwara, Y; Fujita, T; Kohno, M; Nakamoto, C; Suzuki, Y

PHYSICAL REVIEW C, VOLUME 65, 014002

Resonating-group study of baryon-baryon interactions for the complete baryon octet: *NN* interaction

Y. Fujiwara,[1] T. Fujita,[1,*] M. Kohno,[2] C. Nakamoto,[3] and Y. Suzuki[4]
[1]*Department of Physics, Kyoto University, Kyoto 606-8502, Japan*
[2]*Physics Division, Kyushu Dental College, Kitakyushu 803-8580, Japan*
[3]*Suzuka National College of Technology, Suzuka 510-0294, Japan*
[4]*Department of Physics, Niigata University, Niigata 950-2181, Japan*
(Received 9 January 2001; published 6 December 2001)

The baryon-baryon interaction for the complete baryon octet is investigated in a unified framework of the resonating-group method which employs the spin-flavor SU_6 wave functions with explicit color degrees of freedom. The interaction Hamiltonian is composed of the phenomenological confinement potential, the color Fermi-Breit interaction with explicit flavor symmetry breaking, and the effective meson-exchange potentials of scalar, pseudoscalar, and vector-meson types, acting between quarks. For the scalar- and vector-meson exchanges, the momentum-dependent higher-order terms are incorporated to reduce the attractive effect of the central interaction at higher energies. The single-particle potentials of the octet baryons, predicted by the *G*-matrix calculation, now have proper repulsive behavior in the momentum region $q_1=5-20$ fm^{-1}. A moderate contribution of the spin-orbit interaction from the scalar-meson exchange is also included. As to the vector mesons, a dominant contribution is the quadratic spin-orbit force generated from the ρ-meson exchange. This paper discusses the nucleon-nucleon interaction up to $T_{\rm lab}=800$ MeV. The nucleon-nucleon phase shifts at the nonrelativistic energies up to $T_{\rm lab}=350$ MeV are greatly improved, and now have attained the accuracy almost comparable to that of one-boson-exchange potentials. The deuteron properties and the low-energy observables of the nucleon-nucleon interaction are examined in the particle basis by incorporating the isospin symmetry breaking through the mass difference of the neutral and charged pions and the Coulomb effect as well. The nuclear saturation properties and the single-particle potential of the nucleon in symmetric nuclear matter are examined through the *G*-matrix calculation which uses the quark-exchange kernel directly.

DOI: 10.1103/PhysRevC.65.014002 PACS number(s): 13.75.Cs, 13.75.Ev, 12.39.Jh, 21.65.+f

I. INTRODUCTION

One of the purposes of studying the baryon-baryon interaction in the quark model is to obtain the most accurate understanding of the fundamental strong interaction in a natural picture, in which the short-range part of the interaction is relevantly described by the quark-gluon degree of freedom and the medium- and long-range parts of the interaction are dominated by the meson-exchange processes. We have recently achieved a simultaneous and realistic description of the nucleon-nucleon (NN) and hyperon-nucleon (YN) interactions in the resonating-group method (RGM) for the spin-flavor SU_6 quark model [1–5]. In this approach the effective quark-quark (qq) interaction is built by combining a phenomenological quark-confining potential and the colored version of the Fermi-Breit (FB) interaction with minimum effective meson-exchange potentials (EMEP's) of scalar and pseudoscalar meson nonets directly coupled to quarks. Owing to the explicit introduction of quark degrees of freedom, this framework is versatile enough to extend our vast knowledge of the NN interaction to the YN, YY interactions, and more generally to B_8B_8 interactions between the complete octet (B_8) baryons, by utilizing the fact that the nucleons and hyperons belong to a common class of the spin-flavor SU_6 supermultiplet 56. The flavor symmetry breaking in the strangeness systems is explicitly introduced through the quark-mass dependence of the Hamiltonian and the well-established baryon and meson masses. An advantage of introducing the EMEP at the quark level lies in the stringent relationship of the flavor dependence appearing in the various interaction pieces. Accurate description of the NN interaction diminishes the ambiguity of model parameters, which is crucial since the present experimental data for the YN interaction are still very scarce.

In this study we first upgrade our model [1–5] by incorporating such interaction pieces provided by scalar and vector mesons as the spin-orbit (LS), quadratic spin-orbit (QLS), and the momentum-dependent Bryan-Scott terms. Introduction of these pieces to the EMEP is primarily motivated by the insufficient description of the experimental data by previous models. First, some discrepancy of the NN phase shifts in previous models requires the introduction of vector mesons. For example, the $^3D_2$ phase shift in the model FSS [4] is more attractive than experiment by 10° around $T_{\rm lab}\sim 300$ MeV. This implies that the one-pion tensor force is too strong in our previous models. In the standard one-boson-exchange potentials (OBEP's), the strong one-pion tensor force is partially weakened by the ρ meson tensor force. We use the QLS force of vector mesons from the reasons given below. Furthermore, some phase shifts of other partial waves deviate from the empirical ones by a couple of degrees. Another improvement is required as for

*Present address: Japan Meteorological Agency, Chiyoda-ku Tokyo 100, Japan.

the central attraction. The G-matrix calculation using the quark-exchange kernel explicitly [6] shows that energy-independent attraction, dominated by ϵ-meson exchange, is unrealistic, since in our previous models the single particle (s.p.) potentials in symmetric nuclear matter show a strongly attractive behavior in the momentum region $q_1 = 5-20$ fm^{-1}. We have shown in [7] that this flaw can be removed by introducing the momentum-dependent higher-order term of scalar-meson exchange potentials, the importance of which was first pointed out by Bryan and Scott [8]. In the higher-energy region, the LS term of the scalar mesons also makes an appreciable contribution, in addition to this momentum-dependent term.

Another purpose of the present investigation is to examine the charge symmetry breaking (CSB) and the Coulomb effect from the viewpoint of the quark model. It is well known that the $^1S_0$ phase shift of the pp interaction is slightly less attractive than that of the np interaction. This charge independence breaking (CIB) is partially explained by the so-called pion-Coulomb correction [9], which implies (1) the small mass difference of the neutron and the proton, (2) the mass difference of the charged pion and the neutral pion, and (3) the Coulomb effect. Furthermore, it was claimed long ago that the Λp interaction should be more attractive than the Λn interaction, since the binding energy of the 0^+ ground state of $^4_\Lambda$He is fairly larger than that of $^4_\Lambda$H [10]. The CSB energy of 350 keV in these isodoublet hypernuclei is much larger than the ~ 100 keV CSB effect seen in the ^{3}H-^{3}He binding energy difference after the correction of the pp Coulomb energy in ^{3}He is made. The early version of the Nijmegen potential [11] already focused on this CSB in the OBEP including the pion-Coulomb correction and the correct threshold energies of the ΛN-ΣN coupling in the particle basis. The RGM calculation using the particle basis is rather cumbersome, since all the spin-flavor factors of the quark-exchange kernel should be recalculated by properly incorporating the z components of the isospin quantum numbers. Furthermore, there is a problem inherent in the RGM formalism: the internal energies of the clusters are usually not properly reproduced when a unique model Hamiltonian is used. We have given in [12] a convenient prescription to avoid this problem without spoiling the exact antisymmetrization effect of the Pauli principle. For the Coulomb effect, we calculate the full exchange kernel without any approximation. The pion-Coulomb correction and the correct treatment of the threshold energies in the particle basis are found to be very important for the detailed description of the low-energy observables in the ΣN-ΛN coupled-channel problem, which we will discuss in the next paper.

With these renovations of EMEP's and the framework, we have redetermined model parameters in the isospin basis to fit the most recent result of the NN phase shifts [13], the deuteron binding energy, the $^1S_0$ NN scattering length, and the low-energy YN total cross section data. This model is named fss2 since it is based on our previous model FSS [3–5]. The agreement of the phase-shift parameters in the NN sector is greatly improved. The model fss2 shares the good reproduction of the YN scattering data and the essential features of the ΛN-ΣN coupling with our previous models [1–5]. Since the model parameters are all fixed, we next extend fss2 to the more general B_8B_8 interactions: namely, the interactions in the strangeness $S=-2$ sector ($\Lambda\Lambda$, ΞN, $\Sigma\Lambda$ and $\Sigma\Sigma$), $S=-3$ sector ($\Xi\Lambda$ and $\Xi\Sigma$), and $S=-4$ sector ($\Xi\Xi$). The result of the YN interaction and these further extensions will be discussed in a forthcoming paper.

It would be appropriate to discuss briefly the main difference between our model and other models developed by several groups. A pedagogical description of the quark cluster model is found in the review article [14] by the Tokyo University group. A complete microscopical calculation incorporating EMEP's acting between quarks is also carried out by the Salamanca group [15,16] for the NN interaction and the Beijing group [17–19] for the NN and YN interactions. These models incorporate chiral-symmetric effective meson-exchange potentials generated from the scalar and pseudoscalar meson exchanges between quarks. Since they use rather small values of the quark-gluon coupling constant $\alpha_S \sim 0.5$ and the harmonic-oscillator width parameter $b \sim 0.5$ fm, their NN interaction is not accurate enough to describe the low partial waves (S wave and P wave) satisfactorily. In the recent Salamanca model [20], the channel coupling effect of the ΔN and $\Delta\Delta$ configurations is explicitly incorporated in order to reproduce the $^3S_1$ and $^1S_0$ phase shifts simultaneously. The LS component in these models is too small, since they do not take into account the ''antisymmetric'' LS term contained in the FB interaction. In the Beijing model [21], a rather large LS contribution from the scalar-meson exchange is assumed. Our model uses a complete FB interaction with explicit flavor symmetry breaking, together with the moderate contribution of the LS component from the scalar mesons. Furthermore, this is the first attempt to introduce the vector mesons in a full microscopic way.

In the next section we first recapitulate the formulation of the $(3q)$-$(3q)$ Lippmann-Schwinger RGM (LS-RGM) [7] and the G-matrix calculation [6] using the quark-exchange kernel directly. Section II B introduces a new EMEP Hamiltonian for fss2 in the momentum representation. This serves to clarify the difference between the present model fss2 and the previous two models, FSS and RGM-H [3–5]. The spatial part of the quark-exchange kernel in the EMEP sector are given in Appendix A. The model parameters determined in the isospin basis are discussed in Sec. II C. Short comments are given in Sec. II D with respect to the special treatment in the particle basis, including the Coulomb force in the momentum representation. Section III presents results and discussions. We first discuss in Sec. III A the NN phase shifts, differential cross sections, and the polarization for the energies $T_{\rm lab} \leqslant 800$ MeV. Special attention is paid to the effect of inelastic channels, which is not taken into account in the present framework. The five invariant amplitudes for the pp scattering are also examined at the highest energy $T_{\rm lab} = 800$ MeV, in order to clarify the behavior of the s.p. potentials in the asymptotic momentum region and to find a clue to the missing ingredients in the present framework. The deuteron properties and the effective-range parameters of the NN system are discussed in Sec. III B. A simple parametrization of the deuteron wave functions is given in Appendix B. The G-matrix calculation using fss2 is presented in Sec.

III C. This includes the discussion of the nuclear saturation curve, the density dependence of the s.p. potentials, and the Scheerbaum factor of the s.p. spin-orbit strength in symmetric nuclear matter. The final section is devoted to a summary.

II. FORMULATION

A. Lippmann-Schwinger formalism for $(3q)$-$(3q)$ RGM and the G-matrix equation

A new version of our quark model employs the Hamiltonian which includes the interactions generated from the scalar (S), pseudoscalar (PS), and vector (V) meson-exchange potentials acting between quarks:

$$H=\sum_{i=1}^{6}\left(m_ic^2+\frac{\boldsymbol{p}_i^2}{2m_i}-T_G\right)+\sum_{i<j}^{6}\left(U_{ij}^{\mathrm{Cf}}+U_{ij}^{\mathrm{FB}}+\sum_{\beta}U_{ij}^{\mathrm{S}\beta}+\sum_{\beta}U_{ij}^{\mathrm{PS}\beta}+\sum_{\beta}U_{ij}^{\mathrm{V}\beta}\right). \tag{2.1}$$

Here U_{ij}^{Cf} is a confinement potential with a quadratic power law, and U_{ij}^{FB} is the full FB interaction with explicit quark-mass dependence. It is important to note that this confinement potential gives a vanishing contribution to the baryon-baryon interaction, since we assume $(0s)^3$ harmonic oscillator wave functions with a common width parameter b for the internal cluster wave functions. Also, all the contributions from the FB interaction are generated from the quark-exchange diagrams, since we assume color-singlet cluster wave functions. These features are all explained in our previous publications [4]. When the calculations are made in the particle basis, the Coulomb force is also introduced at the quark level. The RGM equation for the parity-projected relative wave function $\chi_\alpha^\pi(\boldsymbol{R})$ is derived from the variational principle $\langle\delta\Psi|E-H|\Psi\rangle=0$, and it reads [4]

$$\left[\varepsilon_\alpha+\frac{\hbar^2}{2\mu_\alpha}\left(\frac{\partial}{\partial\boldsymbol{R}}\right)^2\right]\chi_\alpha^\pi(\boldsymbol{R})=\sum_{\alpha'}\int d\boldsymbol{R}'G_{\alpha\alpha'}(\boldsymbol{R},\boldsymbol{R}';E)\chi_{\alpha'}^\pi(\boldsymbol{R}'), \tag{2.2}$$

where $G_{\alpha\alpha'}(\boldsymbol{R},\boldsymbol{R}';E)$ is composed of various pieces of the interaction kernels as well as the direct potentials of EMEP:

$$G_{\alpha\alpha'}(\boldsymbol{R},\boldsymbol{R}';E)=\delta(\boldsymbol{R}-\boldsymbol{R}')\sum_{\beta}\sum_{\Omega}V_{\alpha\alpha'D}^{\Omega\beta}(\boldsymbol{R})+\sum_{\Omega}\mathcal{M}_{\alpha\alpha'}^{\Omega}(\boldsymbol{R},\boldsymbol{R}')-\varepsilon_\alpha\,\mathcal{M}_{\alpha\alpha'}^{N}(\boldsymbol{R},\boldsymbol{R}'). \tag{2.3}$$

The subscript α stands for a set of quantum numbers of the channel wave function; $\alpha=[1/2(11)a_1,1/2(11)a_2]SS_zYII_z;\mathcal{P}$, where $1/2(11)a$ specifies a member of B_8; the spin value 1/2, the SU_3 quantum number in the Elliott notation $(\lambda\mu)=(11)$, and $a\equiv YI$ the flavor label $[N=1(1/2),\ \Lambda=00,\ \Sigma=01$ and $\Xi=-1(1/2)]$, and $\mathcal{P}$ is the flavor-exchange phase [22]. In the systems of identical particles with $a_1=a_2$ and $I_1=I_2$, $\mathcal{P}$ becomes redundant since it is uniquely determined by the total isospin I as $\mathcal{P}=(-1)^{2I_1-I}$. These are the channel specification scheme in the isospin basis. In the particle basis, necessary modification should be made for the flavor degree of freedom. The relative energy ε_α in the channel α is related to the total energy E of the system in the center-of-mass (c.m.) system through $\varepsilon_\alpha=E-E_a^{\mathrm{int}}$. Here $E_a^{\mathrm{int}}=E_{a_1}^{\mathrm{int}}+E_{a_2}^{\mathrm{int}}$ with $a=a_1a_2$. In Eq. (2.3) the sum over Ω for the direct term implies various contributions of interaction types for the meson-exchange potentials, while β specifies the meson species. On the other hand, Ω for the exchange kernel $\mathcal{M}_{\alpha\alpha'}^{\Omega}(\boldsymbol{R},\boldsymbol{R}')$ involves not only the exchange kinetic-energy (K) term but also various pieces of the FB interaction, as well as several components of EMEP. The RGM equation (2.2) is solved in the Lippmann-Schwinger formalism developed in [7] (which we call LS-RGM). In this formalism, we first calculate the basic Born kernel defined through

$$M_{\alpha\alpha'}^{\mathrm{B}}(\boldsymbol{q}_f,\boldsymbol{q}_i;E)=\langle e^{i\boldsymbol{q}_f\cdot\boldsymbol{R}}|G_{\alpha\alpha'}(\boldsymbol{R},\boldsymbol{R}';E)|e^{i\boldsymbol{q}_i\cdot\boldsymbol{R}'}\rangle=\sum_{\beta}\sum_{\Omega}M_{\alpha\alpha'D}^{\Omega\beta}(\boldsymbol{q}_f,\boldsymbol{q}_i)+\sum_{\Omega}M_{\alpha\alpha'}^{\Omega}(\boldsymbol{q}_f,\boldsymbol{q}_i)\mathcal{O}^{\Omega}(\boldsymbol{q}_f,\boldsymbol{q}_i)-\varepsilon_\alpha\,M_{\alpha\alpha'}^{N}(\boldsymbol{q}_f,\boldsymbol{q}_i), \tag{2.4}$$

where ε_α is the relative energy in the final channel (in the prior form). Each component of the Born kernel, Eq. (2.4), is given in terms of the transferred momentum $\boldsymbol{k}=\boldsymbol{q}_f-\boldsymbol{q}_i$ and the local momentum $\boldsymbol{q}=(\boldsymbol{q}_f+\boldsymbol{q}_i)/2$. In Eq. (2.4) the space-spin invariants $\mathcal{O}^{\Omega}=\mathcal{O}^{\Omega}(\boldsymbol{q}_f,\boldsymbol{q}_i)$ are given by $\mathcal{O}^{\mathrm{central}}=1$ and

$$\mathcal{O}^{LS}=i\boldsymbol{n}\cdot\boldsymbol{S},\quad \mathcal{O}^{LS^{(-)}}=i\boldsymbol{n}\cdot\boldsymbol{S}^{(-)},\quad \mathcal{O}^{LS^{(-)}\sigma}=i\boldsymbol{n}\cdot\boldsymbol{S}^{(-)}P_\sigma,$$

with

$$\boldsymbol{n}=[\boldsymbol{q}_i\times\boldsymbol{q}_f],\quad \boldsymbol{S}=\frac{1}{2}(\boldsymbol{\sigma}_1+\boldsymbol{\sigma}_2),\quad \boldsymbol{S}^{(-)}=\frac{1}{2}(\boldsymbol{\sigma}_1-\boldsymbol{\sigma}_2),\quad P_\sigma=\frac{1+\boldsymbol{\sigma}_1\cdot\boldsymbol{\sigma}_2}{2}. \tag{2.5}$$

For the tensor and QLS parts, it would be convenient to take four natural operators defined by

$$\mathcal{O}^{T}=S_{12}(\boldsymbol{k},\boldsymbol{k}),\quad \mathcal{O}^{T'}=S_{12}(\boldsymbol{q},\boldsymbol{q}),\quad \mathcal{O}^{T''}=S_{12}(\boldsymbol{k},\boldsymbol{q}),\quad \mathcal{O}^{QLS}=S_{12}(\boldsymbol{n},\boldsymbol{n}), \tag{2.6}$$

where $S_{12}(\boldsymbol{a},\boldsymbol{b})=(3/2)[(\boldsymbol{\sigma}_1\cdot\boldsymbol{a})(\boldsymbol{\sigma}_2\cdot\boldsymbol{b})+(\boldsymbol{\sigma}_2\cdot\boldsymbol{a})(\boldsymbol{\sigma}_1\cdot\boldsymbol{b})]-(\boldsymbol{\sigma}_1\cdot\boldsymbol{\sigma}_2)(\boldsymbol{a}\cdot\boldsymbol{b})$. The direct Born kernel $M_{\alpha\alpha'D}^{\Omega\beta}(\boldsymbol{q}_f,\boldsymbol{q}_i)$ in Eq. (2.4) is explicitly given in Eq. (2.14). The exchange Born kernel $M_{\alpha\alpha'}^{(\Omega)}(\boldsymbol{q}_f,\boldsymbol{q}_i)$ is given in Appendix B of [7] for the FB interaction and in Appendix A for the EMEP. The LS-RGM equation is given by

$$T_{\gamma\alpha}(\boldsymbol{p},\boldsymbol{q};E)=V_{\gamma\alpha}(\boldsymbol{p},\boldsymbol{q};E)+\sum_{\beta}\frac{1}{(2\pi)^3}\int d\boldsymbol{k}\ V_{\gamma\beta}(\boldsymbol{p},\boldsymbol{k};E)\times\frac{2\mu_\beta}{\hbar^2}\frac{1}{k_\beta^2-k^2+i\varepsilon}\ T_{\beta\alpha}(\boldsymbol{k},\boldsymbol{q};E),\tag{2.7}$$

where the "quasipotential" $V_{\gamma\alpha}(\boldsymbol{p},\boldsymbol{q};E)$ or more generally $V_{\gamma\beta}(\boldsymbol{p},\boldsymbol{q};E)$ is calculated from

$$V_{\gamma\beta}(\boldsymbol{p},\boldsymbol{q};E)=\frac{1}{2}[M^{\mathrm{B}}_{\gamma\beta}(\boldsymbol{p},\boldsymbol{q};E)+(-1)^{S_\beta}\mathcal{P}_\beta M^{\mathrm{B}}_{\gamma\beta}(\boldsymbol{p},-\boldsymbol{q};E)].\tag{2.8}$$

After the standard procedure of the partial-wave decomposition,[1] the LS-RGM equation (2.7) is solved by the Noyes-Kowalski method [23,24]. The singularity at $k=k_\beta$ is avoided by separating the momentum region into two pieces. The intermediate k integral over $0\leqslant k\leqslant k_\beta$ is carried out using the Gauss-Legendre 15-point quadrature formula and the integral over $k_\beta\leqslant k<\infty$ using the Gauss-Legendre 30-point quadrature formula through the mapping $k=k_\beta+\tan(\pi(1+x)/4)$.

The LS-RGM equation (2.7) is straightforwardly extended to the G-matrix equation by a trivial replacement of the free propergator with the ratio of the angle-averaged Pauli operator and the energy denominator:

$$G_{\gamma\alpha}(\boldsymbol{p},\boldsymbol{q};K,\omega)=V_{\gamma\alpha}(\boldsymbol{p},\boldsymbol{q};E)+\sum_{\beta}\frac{1}{(2\pi)^3}\int d\ \boldsymbol{k}\ V_{\gamma\beta}(\boldsymbol{p},\boldsymbol{k};E)\times\frac{Q_\beta(k,K)}{e_\beta(k,K;\omega)}\ G_{\beta\alpha}(\boldsymbol{k},\boldsymbol{q};K,\omega).\tag{2.9}$$

Since a detailed description of this formalism is already given in [6], there is no need to repeat other equations. The formula to calculate the Scheerbaum factor for the s.p. spin-orbit potential by using the G-matrix solution is also given in [25]. We only repeat how we deal with the energy dependence of the quasipotential $V_{\gamma\alpha}(\boldsymbol{p},\boldsymbol{q};E)$ in the G-matrix equation (2.9). The total energy of the two interacting particles in the nuclear medium is not conserved. Since we only need the diagonal G matrices for calculating s.p. potentials and the nuclear-matter properties in the lowest-order Brueckner theory, we simply use

$$\varepsilon_\gamma=E_a^{\mathrm{int}}-E_c^{\mathrm{int}}+\frac{\hbar^2}{2\mu_\alpha}q^2,\tag{2.10}$$

both in $V_{\gamma\alpha}(\boldsymbol{p},\boldsymbol{q};E)$ and $V_{\gamma\beta}(\boldsymbol{p},\boldsymbol{k};E)$ in Eq. (2.9). The meaning and the adequacy of this procedure are discussed in [12] by using a simple model.

[1]We use the Gauss-Legendre 20-point quadrature formula to carry out the numerical integration for the partial-wave decomposition of Eq. (2.8).

B. Effective meson-exchange potentials for fss2

The EMEP at the quark level is most easily formulated in the momentum representation by using second-order perturbation theory with respect to the quark-baryon vertices. We employ the following qq interaction, which is obtained through the nonrelativistic reduction of the one-boson-exchange amplitudes in the parameter $\gamma=(m/2m_{ud})$ (where m is the exchanged meson mass and m_{ud} is the up-down quark mass):

$$U^{\mathrm{S}}(\boldsymbol{q}_f,\boldsymbol{q}_i)=gg^\dagger\frac{4\pi}{\boldsymbol{k}^2+m^2}\left\{-1+\frac{\boldsymbol{q}^2}{2m_{ud}^2}-\frac{1}{2m_{ud}^2}i\boldsymbol{n}\cdot\boldsymbol{S}\right\},$$

$$U^{\mathrm{PS}}(\boldsymbol{q}_f,\boldsymbol{q}_i)=-ff^\dagger\frac{1}{m_{\pi^+}^2}\frac{4\pi}{\boldsymbol{k}^2+m^2}\left[(\boldsymbol{\sigma}_1\cdot\boldsymbol{k})(\boldsymbol{\sigma}_2\cdot\boldsymbol{k})-(1-c_\delta)\times(m^2+\boldsymbol{k}^2)\frac{1}{3}(\boldsymbol{\sigma}_1\cdot\boldsymbol{\sigma}_2)\right],$$

$$U^{\mathrm{V}}(\boldsymbol{q}_f,\boldsymbol{q}_i)=\frac{4\pi}{\boldsymbol{k}^2+m^2}\left\{f^ef^{e\dagger}\left(1+\frac{3\boldsymbol{q}^2}{2m_{ud}^2}\right)-f^mf^{m\dagger}\frac{2}{(m_{ud}m)^2}\times\left[(\boldsymbol{\sigma}_1\cdot\boldsymbol{n})(\boldsymbol{\sigma}_2\cdot\boldsymbol{n})-(1-c_{qss})\frac{1}{3}\boldsymbol{n}^2(\boldsymbol{\sigma}_1\cdot\boldsymbol{\sigma}_2)\right]-(f^mf^{e\dagger}+f^ef^{m\dagger})\frac{2}{m_{ud}m}i\boldsymbol{n}\cdot\boldsymbol{S}\right\}.\tag{2.11}$$

Here $\boldsymbol{k}=\boldsymbol{q}_f-\boldsymbol{q}_i$, $\boldsymbol{q}=(1/2)(\boldsymbol{q}_f+\boldsymbol{q}_i)$, and the quark-meson coupling constants are expressed in the operator form in the flavor space [26,27]. For example, the product of the two different coupling-constant operators g and f are expressed as

$$gf^\dagger=\begin{cases}g_1f_1\\ g_8f_8\Sigma_a\lambda_a(i)\lambda_a(j)\end{cases}\quad\text{for}\quad\begin{cases}\text{singlet mesons,}\\ \text{octet mesons,}\end{cases}\tag{2.12}$$

where $\lambda_a(i)$ represents the Gell-Mann matrix for particle i. For the realistic description, the meson mixing between the flavor singlet and octet mesons is very important. This implies using

$$f_{\eta'}=f_1\cos\theta+f_8\sin\theta\lambda_8,\quad f_\eta=-f_1\sin\theta+f_8\cos\theta\lambda_8,\tag{2.13}$$

instead of f_1 and $f_8\lambda_8$ in Eq. (2.12) for the PS mesons. Similar transformation is also applied to the S-meson and V-meson coupling constants. The SU_3 parameters of the EMEP coupling constants are therefore f_1, f_8, and θ. The S-meson exchange EMEP in Eq. (2.11) involves not only the attractive leading term, but also the momentum-dependent $\boldsymbol{q}^2$ term and the LS term. The PS-meson exchange operator is the same as before, but the parameter c_δ is introduced only for the one-pion exchange in order to reduce the very strong effect of the delta-function-type contact term involved in the spin-spin interaction. The case $c_\delta=1$ corresponds to the full expression, while $c_\delta=0$ corresponds to the case with no

spin-spin contact term. The V-meson exchange potential is composed of the electric-type term, the magnetic-type term, and the cross term. In the electric term, the central force generated by the ω-meson-exchange potential is usually most important, and it also includes the $\boldsymbol{q}^2$-type momentum-dependent term. As to the introduction of the vector-meson EMEP to the quark model, some discussion already addressed the problem of double counting, especially with the strong short-range repulsion originating from the time component of the ω-meson exchange [28]. We avoid this double counting for the short-range repulsion and the LS force by simply choosing appropriate coupling constants for vector mesons, i.e., f_1^{Ve}, $f_1^{\mathrm{Vm}}\sim 1$, and $f_8^{\mathrm{Ve}}=0$. The magnetic term is usually important for the isovector ρ meson and yields the spin-spin, tensor, and QLS terms in the standard OBEP. The choice in Eq. (2.11) is to keep only the QLS term with the partial contribution of the spin-spin term proportional to $\boldsymbol{L}^2$, the reason for which is discussed below. Finally, the cross term between the electric and magnetic coupling constants leads to the LS force for the qq interaction. The antisymmetric LS $(LS^{(-)})$ force with $\boldsymbol{S}=(\boldsymbol{\sigma}_1-\boldsymbol{\sigma}_2)/2$ is not generated from EMEP's at the quark level, because the flavor operator in Eq. (2.12) is the Gell-Mann matrix and also because the mass difference between the up-down and strange quark masses is ignored in Eq. (2.11).

We should keep in mind that these EMEP's, except for the pions, are by no means a theoretical consequence of the real meson-exchange processes taking place between quarks. First of all, the static approximation used to derive the meson-exchange potentials between quarks is not permissible, since the masses of S mesons and V mesons are more than twice as heavy as the quark mass m_{ud} $\sim$300–400 MeV. Since the parameter γ is not small, the nonrelativistic reduction is not justified. Also, the very strong S-meson central attraction is just a replacement of the real processes of the 2π exchange, the $\pi\rho$ exchange, the Δ excitations, and so forth. The V mesons are supposed to behave as composite particles of the $(q\bar{q})$ pairs. Furthermore, the choice of terms in Eq. (2.11) is quite *ad hoc* and phenomenological. We should consider Eq. (2.11) as an effective interaction to simulate the residual interaction between quarks, which is not taken into account by the FB interaction.

The calculation of the full Born kernel in Eq. (2.4) for each term of Eq. (2.11) becomes rather involved, if we use the standard technique of calculating the exchange kernel in the generator-coordinate kernel (GCM kernel). This becomes especially tedious when the qq interaction involves the nonstatic $\boldsymbol{q}^2$ dependence and the second-order term of $\boldsymbol{q}$ as in the QLS force. We have developed in [7] a new technique to calculate the Born kernel directly from the two-body interaction in the momentum representation. In this technique, there is no need to calculate the GCM kernel. Since the final expression is rather lengthy for the exchange kernel, it is relegated to Appendix A. Here we only show the direct term, which is particularly useful to see the main characteristics of the EMEP introduced in the present model:

$$M_D^{\mathrm{S}}(\boldsymbol{q}_f,\boldsymbol{q}_i)=g^2\frac{4\pi}{\boldsymbol{k}^2+m^2}e^{-(b\boldsymbol{k})^2/3}\left\{X_{0D_+}^{C}\left[-1+\frac{1}{2(3m_{ud})^2}\left(\boldsymbol{q}^2+\frac{9}{2b^2}\right)\right]-\frac{3}{2(3m_{ud})^2}X_{0D_+}^{LS}i\boldsymbol{n}\cdot\boldsymbol{S}-\frac{3}{2(3m_{ud})^2}X_{0D_+}^{LS^{(-)}}i\boldsymbol{n}\cdot\boldsymbol{S}^{(-)}\right\},$$

$$M_D^{\mathrm{PS}}(\boldsymbol{q}_f,\boldsymbol{q}_i)=-f^2\frac{1}{m_{\pi^+}^2}\frac{4\pi}{\boldsymbol{k}^2+m^2}e^{-(b\boldsymbol{k})^2/3}X_{0D_+}^{T}\left[(\boldsymbol{\sigma}_1\cdot\boldsymbol{k})(\boldsymbol{\sigma}_2\cdot\boldsymbol{k})-(1-c_\delta)(m^2+\boldsymbol{k}^2)\frac{1}{3}(\boldsymbol{\sigma}_1\cdot\boldsymbol{\sigma}_2)\right],$$

$$\begin{aligned}M_D^{\mathrm{V}}(\boldsymbol{q}_f,\boldsymbol{q}_i)=\frac{4\pi}{\boldsymbol{k}^2+m^2}e^{-(b\boldsymbol{k})^2/3}\Bigg\{&(f^e)^2\;X_{0D_+}^{C}\left[1+\frac{3}{2(3m_{ud})^2}\left(\boldsymbol{q}^2+\frac{9}{2b^2}\right)\right]-(f^m)^2\frac{2}{(3m_{ud}m)^2}X_{0D_+}^{T}\\&\times\left[(\boldsymbol{\sigma}_1\cdot\boldsymbol{n})(\boldsymbol{\sigma}_2\cdot\boldsymbol{n})-(1-c_{qss})\left(\frac{\boldsymbol{n}^2}{3}+\frac{\boldsymbol{k}^2}{b^2}\right)(\boldsymbol{\sigma}_1\cdot\boldsymbol{\sigma}_2)+\frac{3}{2b^2}[\boldsymbol{\sigma}_1\times\boldsymbol{k}]\cdot[\boldsymbol{\sigma}_2\times\boldsymbol{k}]\right]\\&-2f^mf^e\frac{2}{3m_{ud}m}X_{0D_+}^{LS}i\boldsymbol{n}\cdot\boldsymbol{S}-2f^mf^e\frac{2}{3m_{ud}m}X_{0D_+}^{LS^{(-)}}i\boldsymbol{n}\cdot\boldsymbol{S}^{(-)}\Bigg\}.\end{aligned}\tag{2.14}$$

Here $X_{0D_+}^{\Omega}$ represents the spin-flavor factors related to the spin-flavor operators in Eq. (2.11). The singlet-octet meson mixing, Eq. (2.13), etc., are not explicitly shown because of the typographical reason. The Gaussian factor $\exp\{-(b\boldsymbol{k})^2/3\}$ appearing in Eq. (2.14) represents the form factor effect of the $(0s)^3$ cluster wave functions. The finite size effect of the baryons also appears as the constant zero-point oscillation terms accompanied with the $\boldsymbol{q}^2$ terms, appearing in the S- and V-meson contributions. For the QLS force, the same effect appears as the tensor force having the form $[\boldsymbol{\sigma}_1\times\boldsymbol{k}]\cdot[\boldsymbol{\sigma}_2\times\boldsymbol{k}]$. The magnitude of this term is about one-third if we compare this with the strength from the original tensor term appearing at the level of qq interaction. The advantage of using the QLS force in Eq. (2.11), instead of

the tensor force, is that we can avoid the π-ρ cancellation of the tensor force for the coupling term of the S and D waves. The ϵ_1 parameter of the NN interaction is very sensitive to this coupling strength.

C. Determination of parameters

We have four quark-model parameters: the harmonic-oscillator width parameter b for the $(3q)$ clusters, the up-down quark mass m_{ud}, the strength of the quark-gluon coupling constant α_S, and the mass ratio of the strange to up-down quarks $\lambda=(m_s/m_{ud})$. A reasonable range of the values for these parameters in the present framework is $b=0.5$–0.6 fm, $m_{ud}=300$–400 MeV/c^2, $\alpha_S\sim 2$, and $\lambda=1.2$–1.7. Note that we are dealing with the constituent quark model with explicit mesonic degrees of freedom. The size of the system determined from the $(3q)$ wave function with b [the rms radius of the $(3q)$ system is equal to b] is related to the quark distribution, which determines the range in which the effect of the FB interaction plays an essential role through the quark-exchange kernel. The internal energies of the clusters should be calculated from the same Hamiltonian as used in the two-baryon system and contain not only the quark contribution, but also various EMEP contributions. The value of α_S is naturally correlated with b, m_{ud}, and other EMEP parameters. This implies that α_S in our framework is a parameter which controls the relative importance of the quark contribution and the EMEP contribution, and has very little to do with the real quark-gluon coupling constant of QCD.

For the EMEP part, we have three parameters f_1, f_8, and θ for each of the S, PS, Ve (vector-electric), and Vm (vector-magnetic) terms. It is convenient to use the coupling constants at the baryon level, in order to compare our result with the predictions by other OBEP models. These are related to the coupling constants at the quark level used in Eqs. (2.11) and (2.14) through a simple relationship

$$f_1^{\mathrm{S}}=3g_1,\quad f_8^{\mathrm{S}}=g_8,\quad f_1^{\mathrm{PS}}=f_1,\quad f_8^{\mathrm{PS}}=\frac{5}{3}f_8,$$

$$f_1^{\mathrm{Ve}}=3f_1^e,\quad f_8^{\mathrm{Ve}}=f_8^e,\quad f_1^{\mathrm{Vm}}=f_1^m,\quad f_8^{\mathrm{Vm}}=\frac{5}{3}f_8^m. \tag{2.15}$$

Through this replacement, the leading term for each meson in Eq. (2.14) precisely coincides with that of the OBEP with Gaussian form factors. In the present framework, the S-meson masses are also considered to be free parameters within some appropriate ranges. We further introduce three extra parameters: c_δ the strength factor for the delta-function-type spin-spin contact term of the one-pion-exchange potential (OPEP), c_{qss} the strength factor for the spin-spin term of the QLS force, and c_{qT} the strength factor for the tensor term of the FB interaction. These parameters are introduced to improve the fit of the NN phase shifts to the empirical data, the values of which are fixed throughout in the whole calculations of the B_8B_8 interactions.

We determine these parameters by fitting the most recent result of the phase shift analysis SP99 [13] for the np scattering with the partial waves $J\leqslant 2$ and the incident energies $T_{\mathrm{lab}}\leqslant 350$ MeV, under the constraint of the deuteron binding energy and the $^1S_0$ NN scattering length, as well as to reproduce the available data for the low-energy YN total cross sections. The result is shown in Table I. The parameters of the previous model FSS are also shown for comparison. The χ^2 value used in the parameter search is defined through

$$\sqrt{\chi^2}=\left\{\frac{1}{N}\sum_{i=1}^{N}(\delta_i^{cal}-\delta_i^{expt})^2\right\}^{1/2}, \tag{2.16}$$

where no experimental error bars are employed because the energy-dependent solution of the phase-shift analysis does not give them. In Eq. (2.16) the sum over $i=1$-N is with respect to various angular momenta and energies, and the mixing parameters ϵ_1 and ϵ_2 are also included in the unit of degrees. The value $\sqrt{\chi^2}$ therefore gives some measure for the averaged deviation of the calculated phase shifts from the empirical values. Using the parameter set in Table I, we have obtained $\sqrt{\chi^2}=0.656°$ for the np scattering. The best solution in our previous models is $\sqrt{\chi^2}\sim 3°$ in FSS. Since the present model fss2 is a renovated version of FSS, we summarize in the following only the changes and new points of fss2, in comparison with the model FSS.

(1) In the original expression of the meson-exchange potentials between quarks, the momentum-dependent Bryan-Scott term appears in the combination of $\boldsymbol{q}^2-\boldsymbol{k}^2/4$ for the S meson and $3\boldsymbol{q}^2-\boldsymbol{k}^2/4$ for the V meson. We find that these $\boldsymbol{k}^2/4$ terms (usually replaced by $\boldsymbol{k}^2=-m^2$) play a rather characterless role in making the whole interaction slightly repulsive. With these terms, the energy dependence of the $^1S_0$ and $^3S_1$ phase shifts becomes too strong to keep the value of b in the reasonable range. (The value of b turns out to be too small, about $b\sim 0.4$ fm to compensate the strong energy dependence.) We therefore drop all these $\boldsymbol{k}^2/4$ terms in the present calculation.

(2) We ignore the QLS force from the S mesons, since it is very weak. The S-meson EMEP direct term therefore consists of the leading term with -1 in Eq. (2.14), the momentum-dependent Bryan-Scott term, and the LS term. (For the YN interaction, etc., a small $LS^{(-)}$ contribution emerges at the baryon level from the flavor-octet S mesons.) This LS term yields an appreciable contribution at medium and higher energies, which consequently reduces the value of b from the previous value $\geqslant 0.6$ fm to a smaller value ~ 0.56 fm.

(3) The reduction of the spin-spin contact term for the PS mesons is introduced only for the pion with the smallest mass. For the other heavier PS mesons, we assume the full strength factor $c_\delta=1$. The reduction from 1 for the pion improves the fit of the NN $^1P_1$ phase shift to a great extent. (Otherwise, the repulsion at higher energies is insufficient for this partial wave.) We introduce c_δ only for pion, since the effect of the present $(3q)$-cluster folding corresponds to a very low value of the cutoff mass $\Lambda\sim 800$–900 MeV for the pion form factor in the OBEP. It is well known that such a

TABLE I. Quark-model parameters, SU_3 parameters of the EMEPs, S-meson masses, and some reduction factors c_δ, etc., for the models fss2 and FSS. The ρ meson in fss2 is treated in the two-pole approximation, for which m_1 (β_1) and m_2 (β_2) are shown below the table.

	b (fm)	m_{ud} (MeV/c^2)	α_S	$\lambda = m_s/m_{ud}$
fss2	0.5562	400	1.9759	1.5512
FSS	0.616	360	2.1742	1.526
	f_1^S	f_8^S	θ^S	θ_4^S [a]
fss2	3.48002	0.94459	33.3295°	55.826°
FSS	2.89138	1.07509	27.78°	65°
	f_1^{PS}	f_8^{PS}	θ^{PS}	
fss2	–	0.26748	–	(no η, η')
FSS	0.21426	0.26994	−23°	
	f_1^{Ve}	f_8^{Ve}	f_1^{Vm}	f_8^{Vm} [b]
fss2	1.050	0	1.000	2.577
(MeV/c^2)	m_ϵ	m_{S*}	m_δ	m_κ
fss2	800	1250	846 [c]	936
FSS	800	1250	970	1145
	c_δ	c_{qss}	c_{qT} [e]	
fss2	0.4756 [d]	0.6352	3.139	
FSS	0.381	–	–	

[a] θ_4^S is used only for $\Sigma N(I=3/2)$.
[b] $\theta^V = 35.264°$ (ideal mixing) and two-pole ρ meson with m_1 (β_1) = 664.56 MeV/c^2 (0.34687) and m_2 (β_2) = 912.772 MeV/c^2 (0.48747) [30] are used.
[c] For the NN system, $m_\delta = 720$ MeV/c^2 is used.
[d] Only for π, otherwise 1.
[e] The enhancement factor for the Fermi-Breit tensor term.

low value of Λ converts even the sign of the medium-range part of the OPEP if the full strength of the contact term is introduced. The factor $c_\delta < 1$ also reduces the very strong repulsion generated from the one-pion spin-spin contact term for the S-wave states of the NN system. In the present framework, this repulsion is almost 300 MeV if $c_\delta = 1$ is assumed. Furthermore, the value of c_δ has a strong influence on the internal energies of single baryons. It reduces the very large contribution of the pion to the N-Δ and Λ-Σ mass difference, the latter helping us to keep $\lambda = (m_s/m_{ud})$ at the moderate value. (Otherwise, we obtain $\lambda \sim 1$.) If we do not introduce c_δ and the parameters c_{qss}, c_{qT} discussed below, the $\sqrt{\chi^2}$ value cannot be improved by more than 1.5°. The contribution of η and η' mesons was necessary in the previous models in order to make the ^3S central force relatively more repulsive than the ^1S central force. In the present framework, it turns out that the introduction of these η mesons is not convenient for the subtle balance of the central and tensor forces, especially in the $^3P_2$-$^3F_2$ coupling. We therefore take out all these η-meson contributions. The well-known too-strong repulsion of the NN ^1S central force from the color-magnetic interaction of the FB interaction [17,20] is remedied by assuming two different masses for the isovector δ meson, i.e., $m_\delta = 720$ MeV/c^2 for the NN system and $m_\delta = 846$ MeV/c^2 for the other strangeness systems (see footnote c in Table I).

(4) As is discussed at the end of the preceding subsection, the present model fss2 is the QLS dominant model. This implies that we use the QLS force to reduce the too strong OPEP tensor force, instead of the tensor force itself. The main reason for this choice is that the NN mixing parameter ϵ_1 is very difficult to reproduce if the cancellation of the one pion tensor force and the ρ-meson tensor force is too strong for the S-wave and D-wave coupling. Another question is how this QLS force is incorporated into the model. We find that the QLS spin-spin term $\boldsymbol{n}^2(\boldsymbol{\sigma}_1 \cdot \boldsymbol{\sigma}_2)$ in Eq. (2.11) plays a favorable role in improving the fit of the NN phase shifts. This term corresponds to the $(\boldsymbol{\sigma}_1 \cdot \boldsymbol{\sigma}_2)\boldsymbol{L}^2$ term in the Hamada-Johnstone potential [29]. Since the full introduction of this term results in too vigorous behavior, we introduce a reduction factor c_{qss}, the value of which turns out around $c_{qss} \sim 0.6$. The two-pole formula for the ρ-meson-exchange potential, introduced in [30], is found to give a favorable result. We further find that the short-range tensor force is still too weak. We avoid this difficulty simply by increasing the strength of the tensor term of the FB interaction with the factor c_{qT}. The value $c_{qT} \sim 3$ seems to be reasonable. If we

carry out the parameter search with $c_{qT}=1$, the value of $\sqrt{\chi^2}$ cannot be improved by more than 1.3°–1.0°, mainly due to the disagreement of ϵ_1. We should note, however, that the introduction of the V mesons is a rather minor change from our previous models. With the exception of $f_8^{\mathrm{Vm}}=2.577$, the V-meson coupling constants in Table I are around 1, which is less than half of the coupling constants in the standard OBEP. In particular, the isospin-dependent LS force from the ρ meson is exactly zero, since f_8^{Ve} is fixed at zero. The short-range repulsion in the NN interaction is still mainly described by the color-magnetic term of the FB interaction. The dominant effect of the V mesons is almost solely the ρ-meson QLS force, which is the reason we call fss2 the QLS dominant model.

(5) The following five parameters in Table I are directly related to the reproduction of the low-energy YN cross sections: $\lambda=(m_s/m_{ud})$, θ^{S}, θ_4^{S}, m_δ, and m_κ. Among them, the angle of the singlet-octet meson mixing θ^{S} of the S mesons is used to control the relative strength of the central attraction of the NN and YN interactions. It was found before [4] that, once the θ^{S} is determined to fit the low-energy Λp cross section data, the attraction of the $\Sigma N(I=3/2)$ channel is too strong and the $\Sigma^+ p$ total cross sections are overestimated. We therefore use a larger value for θ^{S} (which is denoted by θ_4^{S}) only for the $\Sigma N(I=3/2)$ channel in order to reduce the attraction, which is the same prescription employed in the previous models [3,4].

(6) The largest ambiguity for determining the parameters related to the YN interaction lies in the strength of the central attraction in the $\Sigma N(I=1/2)$ $^3S_1$ channel [7]. If the phase-shift rise of the $^3S_1$ state is less than 30°, the low-energy $\Sigma^- p$ elastic total cross section becomes too small. If this attraction is too strong, as in RGM-F [2], the $^3S_1$ phase shift shows a sudden decrease from 180° to 60°–90°, and the behavior of the Λp total cross sections at the ΣN threshold becomes a round peak, instead of the cusp structure [31]. Furthermore, the strength of the central attraction plays a crucial role even for the odd-parity state. The $\Sigma N(I=1/2)$ $^3P_1$ phase shift is attractive due to the exchange kinetic-energy kernel: i.e., the effect of the Pauli principle [22]. This attraction is reinforced by the LS force in the diagonal channel and also by the $LS^{(-)}$ force acting between this channel and the $^1P_1$ channel. This channel coupling also takes place between the $\Sigma N(I=1/2)$ channel and the ΛN channel. This channel coupling is mainly determined by the strength of the $LS^{(-)}$ force, which is directly related to the magnitude of α_S, but also considerably influenced by the strength of the central attraction in the $\Sigma N(I=1/2)$ channel. In [7], we have clarified that the central attraction of the previous models RGM-F and FSS is so strong that the $\Sigma N(I=1/2)$ $^3P_1$ resonance is moved to the ΛN $^1P_1$ channel. The consequence of this behavior is the strong enhancement of the Λp total cross sections in the cusp region. On the contrary, the P-wave coupling in the model RGM-H is less strong, and the agreement of the Λp total cross sections to some available experimental data is much better. [See Fig. 10(a) of [4] and Table II of [7].] Here we assume that the resonance stays in the original $\Sigma N(I=1/2)$ $^3P_1$ channel and try to find the parameter set which gives the maximum strength of the $\Sigma N(I=1/2)$ central attraction. In practice, we assume $\sqrt{2/\pi}\alpha_S x^3 m_{ud}c^2=440$ MeV [$x=(\hbar/m_{ud}cb)$ is the ratio of the Compton wavelength of the up-down quarks to b] as in RGM-F and FSS,[2] and adjust the value of m_δ for the YN interaction, independently of the value in the case of NN interaction. If we use a smaller value for m_δ, the $\Sigma N(I=3/2)$ $^1S_0$ state becomes more attractive and the $\Sigma N(I=1/2)$ $^3S_1$ state becomes less attractive.

(7) Another important change from the previous models FSS and RGM-H is the relative strength of the $^1S_0$ and $^3S_1$ attraction in the ΛN interaction. The maximum phase-shift values of the $^1S_0$ and $^3S_1$ states in these models are about 46° and 16°, respectively, around $p_\Lambda\sim 200$ MeV/c. The big difference of almost 30° is known to be unfavorable for the description of the s-shell Λ hypernuclei. Detailed few-body calculations for these hypernuclei have recently been carried out by several groups [32–35] by using various effective ΛN interactions. In these effective ΛN interactions, the effect of the ΣN channel coupling is usually renormalized. These calculations imply that the phase-shift difference of a little less than 10° seems to be most appropriate. We follow this suggestion and adjust the strength of the ΛN attraction such that the $^1S_0$ and $^3S_1$ phase-shift difference is less than 10° and the low-energy Λp cross sections are correctly reproduced. We can use the κ-meson mass to adjust this phase-shift difference. Namely, if m_κ is smaller, then the ΛN $^1S_0$ phase shift becomes more attractive and the $^3S_1$ phase shift becomes less attractive.

In order to give an outline of the framework, we summarize the difference of FSS and fss2 in Table II, with respect to the meson species and interaction types of EMEP's included in the models. Table III shows the quark and EMEP contributions to the baryon mass difference between N and Δ ($\Delta E_{N-\Delta}=E_\Delta^{\mathrm{int}}-E_N^{\mathrm{int}}$) and the mass difference between Λ and Σ ($\Delta E_{\Lambda-\Sigma}=E_\Sigma^{\mathrm{int}}-E_\Lambda^{\mathrm{int}}$), calculated in the isospin basis. We note that various meson contributions largely cancel each other and the net contribution is roughly given by the quark contribution from the color-magnetic term of the FB interaction.

D. Calculation in the particle basis

In this subsection we discuss some new features required in the calculation in the particle basis. Three different types of calculations are carried out in this paper.

(1) Calculation in the isospin basis.

(2) Calculation in the particle basis without the Coulomb force.

(3) Calculation in the particle basis with the Coulomb force.

For the NN interaction, the calculation in the particle basis is rather straightforward. We use the empirical proton and

[2]This value corresponds to assuming the N-Δ mass difference 293.3 MeV only by the FB interaction, as seen from Table III. If we use the α_S value about 1.3 times larger, the transition of the P-wave resonance to the ΛN $^1P_1$ channel takes place in the present model.

TABLE II. The interaction types and the meson species introduced in the EMEPs of the models fss2 and FSS. C represents the central force, SS the spin-spin force, T the tensor force, and QLS the quadratic spin-orbit force. $C(BS)$ implies that the momentum-dependent Bryan-Scott term is also included for the central force. The tensor term of the vector mesons is switched off at the quark level.

Model	Meson type	Interaction type	Mesons
fss2	S	$C(BS)+LS$	ϵ, S^*, δ, κ
	PS	$SS+T$	π, K
	V	$C(BS)+LS+QLS$	ω, ϕ, ρ, K^*
FSS	S	C	ϵ, S^*, δ, κ
	PS	$SS+T$	η', η, π, K

neutron masses ($M_p=938.2723$ MeV and $M_n=939.565$ MeV) and evaluate spin-flavor factors for the charged pion and the neutral pion separately in the isospin representation. The other spin-flavor factors for heavier mesons and the FB interaction are generated in the simple isospin relations. The Coulomb force is introduced at the quark level by using the quark charges. The exchange Coulomb kernel has the same structure as the color-Coulombic term of the FB interaction.

Only complexity arises when we solve the LS-RGM equation in the momentum representation. The standard technique by Vincent and Phatak [36] is employed to solve the Lippmann-Schwinger equation in the momentum representation, including the Coulomb force. This technique requires introducing a cutoff radius R_C for the Coulomb interaction. In the RGM formalism, we have to introduce this cutoff at the quark level, in order to avoid violating the Pauli principle. The two-body Coulomb force assumed in the present calculation is therefore written as

TABLE III. Quark and EMEP contributions to the N-Δ mass difference ($\Delta E_{N-\Delta}$) and the Λ - Σ mass difference ($\Delta E_{\Lambda-\Sigma}$) in MeV, calculated in the isospin basis. The model is fss2. The mass ratio of strange to up-down quarks, $\lambda=(m_s/m_{ud})=1.5512$, is employed to calculate the quark contribution in $\Delta E_{\Lambda-\Sigma}$. The details of the EMEP contribution to $\Delta E_{\Lambda-\Sigma}$ are given in a forthcoming paper. See Table I for the two-pole ρ-meson parameters and the other EMEP parameters.

	β	m_β (MeV/c^2)	E (MeV)
$\Delta E_{N-\Delta}$	Quark		293.33
	δ	720	-164.70
	π	138.039	71.56
	ω	781.940	-34.36
	ϕ	1019.413	-0.19
	ρ	Two pole	80.59
Expt.	293.3	Total	246.23
$\Delta E_{\Lambda-\Sigma}$	Quark	($\lambda=1.5512$)	69.49
	EMEP	$-$	7.98
Expt.	77.44	Total	77.47

$$U_{ij}^{CL}=Q_iQ_je^2\frac{1}{r_{ij}}\Theta(R_C-r_{ij}), \tag{2.17}$$

where Θ is the Heaviside step function and Q_i, $Q_j=2/3$ for the up quark and $-1/3$ for the down and strange quarks. The Coulomb contribution to the internal energies becomes zero for the proton and Σ^+, etc. More explicitly, this can be given by

$$E_{\rm int}^{CL}=X_{0E}^{CL}\sqrt{\frac{2}{\pi}}\alpha x m_{ud}c^2\left\{1-\exp\left[-\frac{1}{2}\left(\frac{R_C}{b}\right)^2\right]\right\}, \tag{2.18}$$

where $\alpha=(e^2/\hbar c)\sim 1/137$ is the hyperfine coupling constant and the direct spin-flavor factor is expressed as $X_{0E}^{CL}=\Sigma_{i=1,2}[Z_i(Z_i-1/3)/2-1/3]$ in terms of the total charge Z_i of the ith baryon. The basic Born kernel for the direct Coulomb term reads

$$M_D^{CL}(\boldsymbol{q}_f,\boldsymbol{q}_i)=Z_1Z_2e^2 2\pi R_C^2\left(\frac{2}{kR_C}\sin\frac{kR_C}{2}\right)^2 e^{-(bk)^2/3}$$

with

$$k=|\boldsymbol{q}_f-\boldsymbol{q}_i|, \tag{2.19}$$

which corresponds to the direct Coulomb potential

$$V_D(r)=Z_1Z_2e^2\frac{1}{r}\left\{\mathrm{erf}(\sqrt{\gamma}r)-\frac{1}{2}\{\mathrm{erf}[\sqrt{\gamma}(r+R_C)]+\mathrm{erf}[\sqrt{\gamma}(r-R_C)]\}\right\}. \tag{2.20}$$

Here $\mathrm{erf}(x)=(2/\sqrt{\pi})\int_0^x e^{-t^2}dt$ stands for the error function and $\gamma=\mu\nu=(3/4b^2)$. The exchange Coulomb kernel is also slightly modified from the exact Coulomb kernel. This is given in Appendix A, together with other EMEP kernels. The value R_C should be sufficiently large to be free from any nuclear effect beyond R_C. Then the final S matrix is calculated from the condition that the wave function obtained by solving the Lippmann-Schwinger equation with the modified Coulomb force is smoothly connected to the asymptotic Coulomb wave function. We take $R_C=9$ fm, although a much smaller value seems to be sufficient. Note that, even in the np and nn systems, we have small contributions from the Coulomb interaction through the exchange Coulomb kernel. The difference between the calculations (2) and (3) for the system of chargeless particles implies this effect.

III. RESULTS AND DISCUSSIONS

A. NN result

Figures 1(a)–1(i) compare the np phase shifts and the mixing angles ϵ_J predicted by fss2 with the recent phase-shift analysis SP99 by Arndt [13]. The parameter search and the calculation of phase-shift parameters in this subsection are all carried out in the isospin basis. For comparison, the previous results by FSS are also shown with the dotted

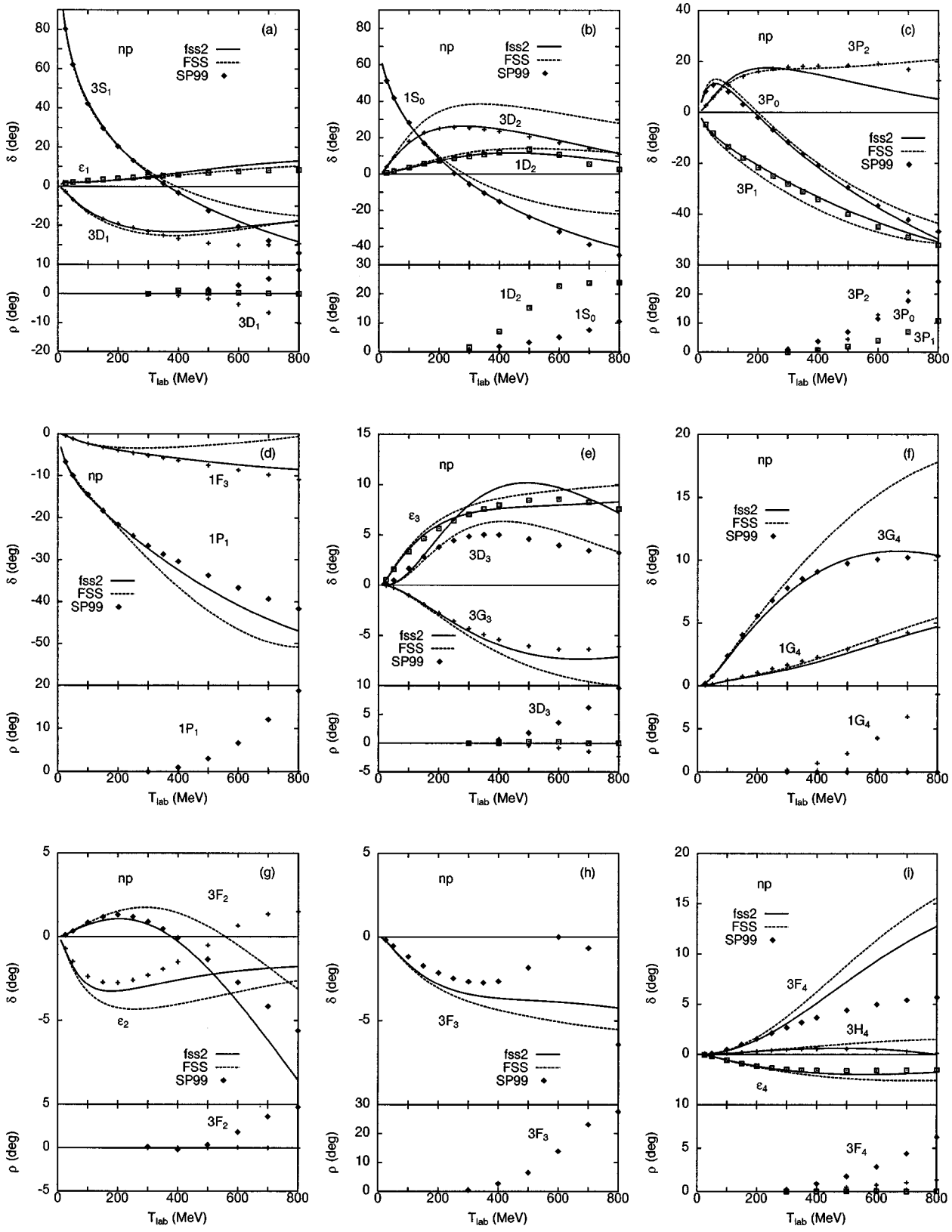

FIG. 1. Calculated np phase shifts by fss2 in the isospin basis, compared with the phase-shift analysis SP99 by Arndt [13]. The dotted curves indicate the result given by FSS. Some empirical inelasticity parameters ρ of SP99 are also shown for $T_{\rm lab} \geqslant 300$ MeV, in order to give a measure of possible deviations of the phase-shift values in the single-channel calculation.

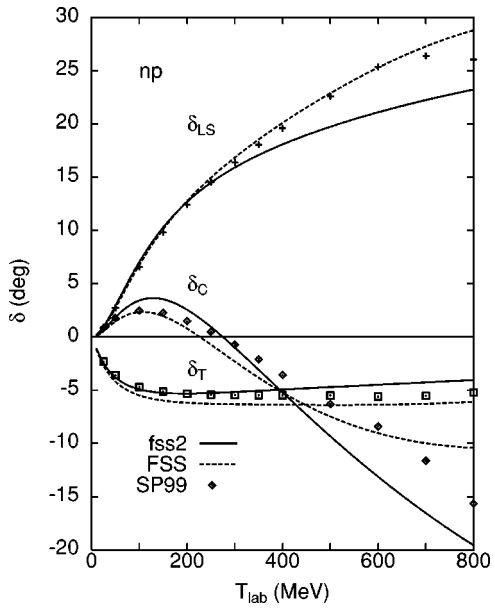

FIG. 2. Decomposition of the ^3P_J phase shifts for the np scattering to the central (δ_C), LS (δ_{LS}), and tensor (δ_T) components. The results given by fss2 (solid curves) and FSS (dashed curves) are compared with the decomposition of the empirical phase shifts SP99 [13].

curves. Here we examine the partial waves up to $J=4$ in the energy range $T_{\rm lab}=0$–800 MeV. For energies higher than 300 MeV, the inelasticity parameters ρ of SP99 are given for a measure of possible deviations of the phase-shift values in the single-channel calculation. The $^3D_2$ phase shift is greatly improved by the QLS component. Even in the other partial waves, the improvement of the phase-shift parameters is usually achieved. This includes (1) $^3P_0$, $^3P_1$, and $^3G_4$ phase shifts, (2) $^3S_1$, $^1S_0$, $^1P_1$, $^1F_3$, and $^3H_4$ phase shifts at higher energies $T_{\rm lab}=400$–800 MeV, and (3) some improvement in $^3F_2$ phase shift and ϵ_2 mixing parameter. On the other hand, $^3P_2$ and $^3D_3$ phase shifts turn out worse and $^3F_4$ phase shift is not much improved. The disagreement of the $^3D_3$ phase shift and the deviation of the $^3D_1$ phase shift at the higher energies imply that our description of the central, tensor, and LS forces in the ^3E states requires further improvement. The insufficiency in the ^3O partial waves is probably related to the imbalance of the central force and the LS force in the short-range region. The decomposition of the ^3P_J phase shifts to the central, LS and tensor components, shown in Fig. 2, implies that the ^3O central force is too repulsive at higher energies $T_{\rm lab}\geqslant 400$–500 MeV. It should be noted that whenever the discrepancy of the phase-shift parameters between the calculation and the experiment is large, the inelasticity parameters are also very large. In particular, the inelasticity parameters of the $^3P_2$, $^1D_2$, and $^3F_3$ states rise very rapidly as the energy increases and reach more than 20° at $T_{\rm lab}=800$ MeV. The elastic phase shift for each of these states shows a dispersionlike resonance behavior at the energy range from 500 MeV to 800 MeV. These are the well-know dibaryon resonances directly related to the ΔN threshold in the isospin $I=1$ channel. The present single-channel calculation is not capable of describing these resonances.

Table IV tabulates the values of phase-shift parameters in the energy range $T_{\rm lab}=25$–300 MeV, in comparison with phase-shift analyses SP99 [13] and PWA93 [37] by the Nijmegen group. The partial waves only up to $J=2$ are considered. If we calculate the χ^2 values Eq. (2.16) using these numbers, we obtain $\sqrt{\chi^2}=0.59°$ and 0.60° for SP99 and PWA93, respectively. We have also calculated the corresponding χ^2 values by using the phase-shift parameters of OBEP, Paris, and Bonn potentials given in Table 5.2 of [38]. We obtain $\sqrt{\chi^2}=1.10°$ (1.08°), 1.41° (1.39°), and 1.32° (1.22°) for OBEP, Paris, and Bonn, respectively, if SP99 (PWA93) is used. The reason we get such results is as follows. In the meson-exchange models, the accuracy of the low-energy phase shifts is less than 0.2°, and the agreement with the experiment is excellent. However, in higher energies the deviation from the experiment increases, and in some particular partial waves like $^1S_0$ and $^3P_0$ states, it becomes more than 2°. In the Paris potential, the $^1S_0$ phase shift is apparently too repulsive. This is, however, because the parameters of the Paris potential are determined by the fit to the pp phase shifts, and the correction due to the CSB is probably not taken into account in the numbers given in Table 5.2 of [38]. Every model has its own weak points. For example, the tensor force of the Bonn potential is usually very weak, which is reflected in the ϵ_1 parameter and in the too attractive behavior of the $^3P_0$ phase shift. (However, the recent CD Bonn potential [9] fits the NN phase-shift parameters in the nonrelativistic energies almost perfectly, with various possible corrections taken into account.) The weak point of our model lies in the $^3P_2$ and $^3D_3$ phase shifts at the intermediate and higher energies $T_{\rm lab}=300$–800 MeV. The empirical $^3P_2$ phase shift gradually decreases if we ignore the weak dispersionlike behavior. Our result, however, decreases too rapidly. Our $^3D_3$ phase shift is too attractive by 4°–6°.

We have examined the differential cross sections and polarizations for the elastic np and pp scatterings, by incorporating the full Coulomb force in the particle basis. The improvements from the previous FSS results given in Figs. 1, 2 of [5] and Figs. 2, 3 of [7] are summarized as follows: (1) the overestimation of the np differential cross sections at the forward angle at $T_{\rm lab}=320$ MeV is corrected, (2) the bump structure of the np differential cross sections around $\theta_{\rm c.m.}=130°$ at energies $T_{\rm lab}=300$–800 MeV has disappeared, (3) the overestimation of the pp differential cross sections at $\theta_{\rm c.m.}=10°$–$30°$ at energies $T_{\rm lab}=140$–400 MeV is improved. However, the essential difficulties of FSS and RGM-H, namely, the oscillatory behavior of the np polarization around $\theta_{\rm c.m.}\sim 110°$ and that of the pp polarization around the symmetric angle $\theta_{\rm c.m.}=90°$ for higher energies $T_{\rm lab}\geqslant 400$ MeV are not resolved. Furthermore, the pp differential cross sections show a deep dip at angles $\theta_{\rm c.m.}\leqslant 30°$ and $\geqslant 150°$ for $T_{\rm lab}\geqslant 500$ MeV. The low-energy pp cross sections at $\theta_{\rm c.m.}=90°$ for $T_{\rm lab}\leqslant 100$ MeV are still overestimated. The differential cross section and polarization plots of fss2 up to $T_{\rm lab}\leqslant 800$ MeV are available upon request.

TABLE IV. Comparison of the np phase-shift parameters calculated in the isospin basis (in degrees) with the phase shift analyses SP99 [13] by Arndt and PWA93 [37] by the Nijmegen group.

State	Model	$T_{\rm lab}$ (MeV)					
		25	50	100	150	200	300
$^3S_1$	fss2	80.98	63.03	43.21	30.51	21.00	7.02
	SP99	80.26	62.10	42.22	29.69	20.51	7.07
	PWA93	80.63	62.77	43.23	30.72	21.22	6.60
$^3D_1$	fss2	−2.82	−6.52	−12.43	−16.59	−19.49	−22.58
	SP99	−2.72	−6.84	−13.09	−16.69	−19.08	−23.04
	PWA93	−2.80	−6.43	−12.23	−16.48	−19.71	−24.14
ϵ_1	fss2	1.68	1.91	2.21	2.68	3.33	4.97
	SP99	1.69	2.14	2.91	3.55	4.08	5.06
	PWA93	1.79	2.11	2.42	2.75	3.13	4.03
$^1P_1$	fss2	−6.70	−10.26	−14.82	−18.38	−21.57	−27.32
	SP99	−6.71	−9.98	−14.47	−18.29	−21.56	−26.62
	PWA93	−6.31	−9.67	−14.52	−18.65	−22.18	−27.58
$^3D_2$	fss2	3.67	8.82	17.09	22.26	25.06	26.38
	SP99	3.87	9.37	17.89	22.73	25.03	25.47
	PWA93	3.71	8.97	17.28	22.13	24.51	25.45
$^1S_0$	fss2	52.26	41.94	27.51	16.91	8.41	−4.86
	SP99	51.30	41.88	28.24	16.95	7.74	−5.49
	PWA93	50.90	40.54	26.78	16.94	8.94	−4.46
$^3P_0$	fss2	8.55	11.25	9.04	4.02	−1.49	−12.10
	SP99	8.24	10.75	8.18	3.15	−1.95	−11.63
	PWA93	8.13	10.70	8.46	3.69	−1.44	−11.47
$^3P_1$	fss2	−5.23	−8.68	−13.45	−17.27	−20.77	−27.26
	SP99	−4.75	−8.15	−13.52	−17.92	−21.64	−28.06
	PWA93	−4.88	−8.25	−13.24	−17.46	−21.30	−28.07
$^1D_2$	fss2	0.64	1.47	3.29	5.30	7.27	10.28
	SP99	0.64	1.59	3.60	5.60	7.33	9.75
	PWA93	0.68	1.73	3.90	5.79	7.29	9.69
$^3P_2$	fss2	2.58	6.26	12.43	15.92	17.36	16.97
	SP99	2.70	5.93	10.92	14.11	16.05	17.83
	PWA93	2.56	5.89	10.94	13.84	15.46	16.95
$^3F_2$	fss2	0.10	0.32	0.72	0.98	1.08	0.75
	SP99	0.09	0.33	0.85	1.19	1.31	0.90
	PWA93	0.09	0.30	0.76	1.12	1.33	1.19
ϵ_2	fss2	−0.82	−1.77	−2.85	−3.22	−3.24	−2.94
	SP99	−0.70	−1.48	−2.37	−2.71	−2.74	−2.29
	PWA93	−0.76	−1.63	−2.58	−2.80	−2.70	−2.30

In order to find a possible reason for the unfavorable oscillations of our polarizations, we show in Fig. 3 the five independent pp invariant amplitudes at the highest energy $T_{\rm lab}=800$ MeV. They are composed of the real and imaginary parts of g_0 (spin-independent central), h_0 (LS), h_n [$(\boldsymbol{\sigma}_1\cdot\hat{\boldsymbol{n}})(\boldsymbol{\sigma}_2\cdot\hat{\boldsymbol{n}})$-type tensor], h_k [$(\boldsymbol{\sigma}_1\cdot\hat{\boldsymbol{k}})(\boldsymbol{\sigma}_2\cdot\hat{\boldsymbol{k}})$-type tensor], and h_P [$(\boldsymbol{\sigma}_1\cdot\hat{\boldsymbol{P}})(\boldsymbol{\sigma}_2\cdot\hat{\boldsymbol{P}})$-type tensor] invariant amplitudes. (See Ref. [7] for the notation.) In Fig. 3 the Coulomb force is neglected in the predictions by the Paris potential. The result by SP99 is calculated using only the real parts of the empirical phase-shift parameters. If we recall that the polarization is given by the cross term contribution of the central, LS, and tensor invariant amplitudes (i.e., $P(\theta)=2\ \mathrm{Im}[(g_0+h_n)(h_0)^*]$; see Eq. (2.32) of [7]) we find that

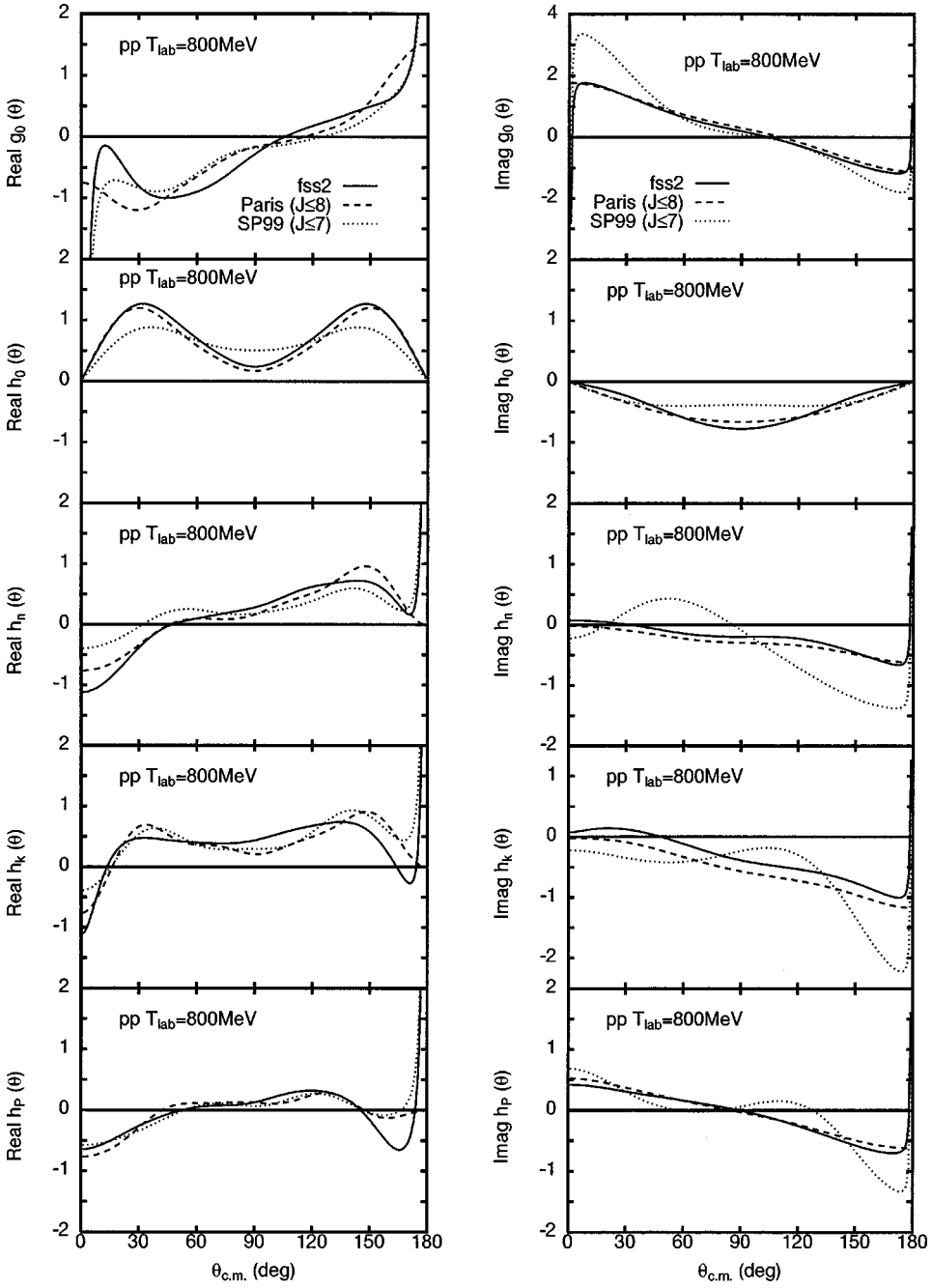

FIG. 3. The five invariant amplitudes for the pp scattering at $T_{\rm lab}=$ 800 MeV, calculated by fss2 (solid curves), the Paris potential [39] (dashed curves), and the empirical phase shifts SP99 [13] (dotted curves). The Coulomb force is included in fss2 and SP99, but not in the Paris potential.

the disagreement in $\mathrm{Im}\,h_n$ and $\mathrm{Re}\,h_0$ with the SP99 result (dotted curves) is most serious. Since the oscillatory behavior of $\mathrm{Im}\,h_n$ in SP99 also appears in $\mathrm{Im}\,h_k$ and $\mathrm{Im}\,h_P$, it is possible that this is an oscillation caused by the NN-ΔN channel coupling through the one pion spin-spin and tensor forces. Figure 3 also shows the reason for the underestimation of the differential cross sections at $\theta_{\rm c.m.}\leqq 30°$. Namely, the imaginary part of g_0 is too small both for fss2 and the Paris potential, and the real part of g_0 is strongly reduced in fss2.

Another application of the invariant amplitudes is the $t^{\rm eff}\rho$ prescription for calculating the s.p. potentials of the nucleons and hyperons in nuclear matter. It is discussed in [7] that the s.p. potentials predicted by the model FSS in the G-matrix calculation show fairly strong attractive behavior in the momentum interval $q_1=5-20$ fm^{-1} for all the baryons. In particular, $U_N(q_1)$ in the continuous prescription becomes almost -80 MeV at $q_1=10$ fm^{-1}. This momentum interval corresponds to the incident energy range $T_{\rm lab}=500$ MeV to 8 GeV in the NN scattering. The $t^{\rm eff}\rho$ prescription is a convenient way to evaluate the s.p. potentials in the asymptotic momentum region in terms of the spin-independent invariant amplitude at the forward angle $g_0(\theta=0)$. Since the present model fss2 incorporates the momentum-dependent Bryan-Scott term, the asymptotic behavior of the s.p. potentials in the large momentum region is improved. We can see this in Fig. 4, where the s.p. potentials of N, Λ, and Σ calculated in the G-matrix approach are shown in the momentum range $q_1=0-10$ fm^{-1}. Figures 4(a) and 4(b) show the result in the QTQ prescription, and Figs. 4(c) and 4(d) in the continuous

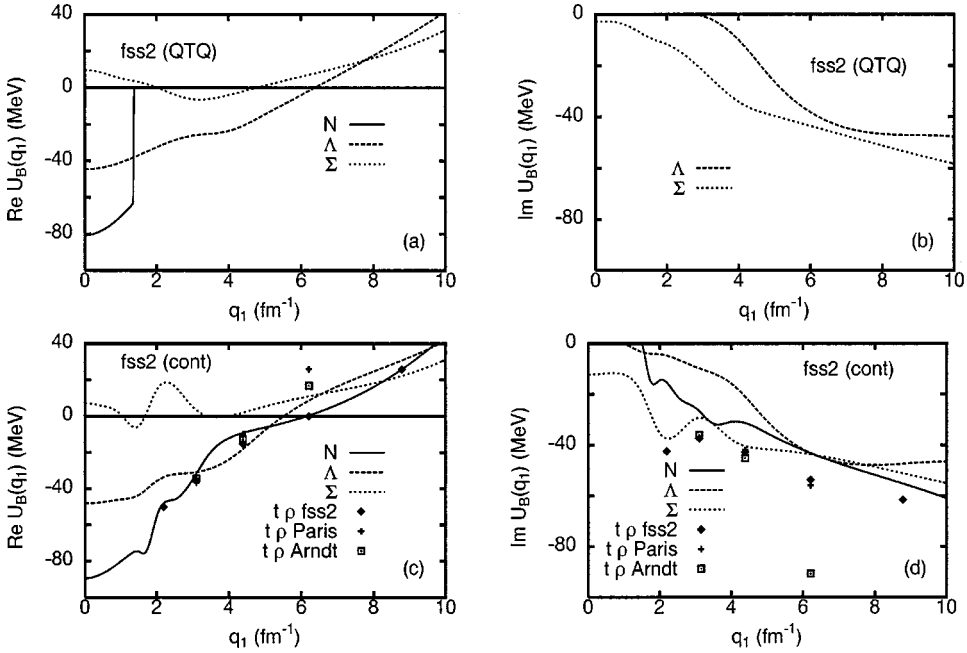

FIG. 4. (a) The momentum dependence of the s.p. potentials $U_B(q_1)$ predicted by the G-matrix calculation of fss2. The QTQ prescription is used for intermediate spectra. The real part Re $U_B(q_1)$ is shown. (b) The same as (a) but for the imaginary part Im $U_B(q_1)$. (c) The same as (a) but in the continuous prescription for intermediate spectra. The nucleon s.p. potentials obtained by the $t^{\rm eff}\rho$ prescription are also shown with respect to the T matrices of fss2, the Paris potential [39], and the empirical phase shifts SP99 [13]. The momentum points selected correspond to $T_{\rm lab}=100$, 200, 400, 800, and 1600 MeV for the NN scattering. The partial waves up to $J\leqslant 8$ are included in fss2 and the Paris potential, and $J\leqslant 7$ in SP99. (d) The same as (c) but for the imaginary part Im $U_B(q_1)$.

choice for intermediate spectra. Figures 4(a) and 4(c) show the real part of $U_B(q_1)$, and Figs. 4(b) and 4(d) the imaginary part. In Figs. 4(c) and 4(d), the solid curves for the nucleon s.p. potential are compared with the results by the $t^{\rm eff}\rho$ prescription with respect to the T matrices of fss2, the Paris potential [39], and the empirical phase shifts SP99 [13]. The partial waves up to $J\leqslant 8$ are included in fss2 and the Paris potential, and $J\leqslant 7$ in SP99. The momentum points calculated correspond to the energies $T_{\rm lab}=100$, 200, 400, 800, and 1600 MeV. We find that the real part of $U_N(q_1)$ nicely reproduces the result of the G-matrix calculation even at such a low energy as $T_{\rm lab}=100$ MeV. On the other hand, the imaginary part by the $t^{\rm eff}\rho$ prescription usually overestimates the exact result especially at the lower energies.

B. Deuteron properties and effective range parameters

The deuteron properties are calculated by solving the LS-RGM equation with respect to the relative wave functions $f_0(k)$ and $f_2(k)$ in the momentum representation (see Appendix B). The properly normalized wave functions in the Schrödinger picture are not $f_l(k)$ but $F_l=\sqrt{N}f_l$, where N represents the normalization kernel [4]. The S-wave and D-wave wave functions in the coordinate representation, $u(R)$ and $w(R)$, are then obtained from the inverse Fourier transform of $F_l(k)$. This process is most easily carried out by expanding $F_l(k)$ in a series of Yukawa functions $\sqrt{2/\pi}k/(k^2+\gamma_j^2)$ in the momentum representation (see Appendix D in [9]). We choose $\gamma_j=\gamma+(j-1)\gamma_0$ with $\gamma_0=0.9$ fm^{-2} and $j=1-11$. The γ is the S-matrix pole $q=-i\gamma$, from which the deuteron energy ϵ_d is most accurately calculated by using the relativistic relation

$$M_n+M_p-\epsilon_d=\sqrt{M_n^2-\gamma^2}+\sqrt{M_p^2-\gamma^2}. \qquad (3.1)$$

Figure 5 shows the deuteron wave functions of fss2 in the coordinate and momentum representations, compared with those of the Bonn model-C potential [38] (dotted curves).[3] We find that the difference between the two models is very small. Table V compares various deuteron properties calculated in three different schemes. They are also compared with the empirical values and the predictions by the Bonn model-C potential. The final value of the deuteron binding energy for fss2 is $\epsilon_d=2.2309$ MeV. If we use the nonrelativistic energy expression[4] $\epsilon_d=(\gamma^2/M_N)$ for $\gamma^2=0.053\,761\,57$ fm^{-2} in the full calculation, we obtain $\epsilon_d=2.2295$ MeV and the difference is 1.4 keV. The differences within the deuteron parameters calculated in the three different schemes are very small, except for the binding energy ϵ_d. In particular, the exchange Coulomb kernel due to the exact antisymmetrization at the quark level gives an attractive effect to the binding energy and increases ϵ_d by 4.8 keV. This is even larger than the relativistic correction in-

[3]The results of the Bonn model-C potential in Fig. 5 and in Table V are based on the parametrized deuteron wave functions given in Table C.4 of [38].

[4]In Table V, the value of ϵ_d in the isospin basis is calculated using this nonrelativistic formula.

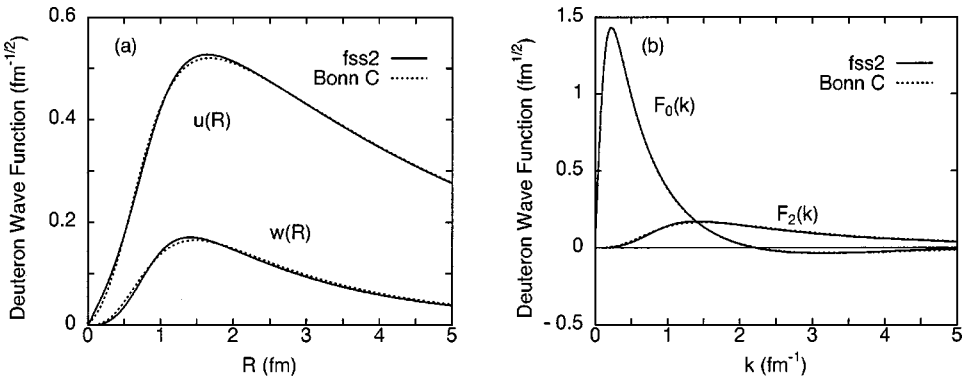

FIG. 5. (a) The deuteron wave functions predicted by fss2 (solid curves) and by Bonn model-C [38] in the coordinate representation. (b) The same as (a) but in the momentum representation.

cluded in Eq. (3.1). The deuteron D-state probability is $P_D = 5.49\%$ in fss2, which is slightly smaller than 5.88% in FSS [4]. These values are rather close to the value $P_D = 5.60\%$ obtained by the Bonn model-C potential [38]. The asymptotic D/S state ratio η and the rms radius are very well reproduced. On the other hand, the quadrupole moment is too small by about 5%–6%. There are some calculations [41,42] which claim that the effect of the meson-exchange currents on the dueteron quadrupole moment is as large as $\Delta Q_d = 0.01$ fm^2. It is noteworthy that the Bonn model-C almost reproduces the correct quadrupole moment, in spite of the fact that the D-state probability is very close to ours. (On the other hand, the quadrupole moment of CD-Bonn [9] is $Q_d = 0.270$ fm^2 with a smaller value $P_D = 4.85\%$.) For the magnetic moment, precise comparison with the experimental value requires a careful estimation of various corrections arising from the meson-exchange currents and the relativistic effect of the current operator, etc.

Table VI lists the S- and P-wave effective range parameters for the NN system, calculated in the three schemes. Since the pion-Coulomb correction is not sufficient to explain the full CIB effect existing in the np and pp $^1S_0$ states, a simple prescription to multiply the flavor-singlet S-meson coupling constant f_1^S by a factor 0.9949 is adopted to reduce the too large attraction of the pp central force. (This prescription is applied only to the calculation in the particle basis.) The underlined values of the scattering length parameter a in Table VI indicate that they are fitted to the experimental values. We find that the pion-Coulomb correction in the np $^1S_0$ state has a rather large effect on a. The value $a = -23.76$ fm in the particle basis changes to $a = -27.38$ fm due to the effect of the pion mass correction and the explicit use of the neutron and proton masses. It further changes to $a = -27.87$ fm due to the small effect of the exchange Coulomb kernel. These changes however should be carefully reexamined by readjusting the binding energy of the deuteron in Table V. We did not carry out this program, since the reduction of f_1^S to fit these values to the empirical value $a = -23.748 \pm 0.010$ fm does not help much to reproduce the CIB of the pp channel anyway. We have to say that the improvement of the NN S-wave effective range parameters in the particle basis calculation is not excellent, in spite of the large effort expended in incorporating the pion-Coulomb correction in the microscopic RGM formalism. This shortcoming might be related to the insufficient description of the low-energy pp differential cross sections around $\theta_{\rm cm} \sim 90°$. It was also pointed out by the Nijmegen group [48] that the Coulomb phase shift should be improved by the effects of two-photon exchange, vacuum polarization, and magnetic moment interactions, in order to describe the $^1S_0$ phase shift precisely at energies less than 30 MeV. These effects are not incorporated in the present calculation. The P-wave effective range parameters are also given in Table VI, in order to compare with a number of empirical predictions. The parameters of $^3P_2$ state are not given, since the effective range expansion of this partial wave requires a correction term related to the accidental p^5 low-energy behavior of the OPEP [49].

C. *G*-matrix calculation

Figure 6 shows saturation curves calculated for ordinary nuclear matter with the QTQ prescription as well as the continuous prescription for intermediate spectra. The

TABLE V. Deuteron properties by fss2 in three different calculational schemes, compared with th predictions of the Bonn model-C potential [38] and the experiment.

	Isospin basis	Particle basis		Bonn C	Expt.	Ref.
		Coulomb off	Coulomb on			
ϵ_d (MeV)	2.2250	2.2261	2.2309	fitted	2.224644 ± 0.000046	[40]
P_D (%)	5.490	5.490	5.494	5.60		
$\eta = A_D/A_S$	0.02527	0.02527	0.02531	0.0266	0.0256 ± 0.0004	[43]
rms (fm)	1.9598	1.9599	1.9582	1.968	1.9635 ± 0.0046	[40]
Q_d (fm^2)	0.2696	0.2696	0.2694	0.2814	0.2860 ± 0.0015	[44]
μ_d (μ_N)	0.8485	0.8485	0.8485	0.8479	0.85742	

TABLE VI. Effective range parameters of fss2 for the NN interaction; the scattering length a, the effective range r, and the shape-dependent parameter P. For the pp and nn systems, the calculation in the particle basis uses $f_1^S \times 0.9949$, in order to incorporate the effect of the charge independence breaking. Unit of length is in fm^{2l+1} in a, fm^{-2l+1} in r, and fm^{-2l} in P for the partial wave l. The experimental values are taken from [40,45–48,9].

		Isospin basis	Particle basis		Expt.
			Coulomb off	Coulomb on	
$pp\ ^1S_0$	a	−23.76	−17.80	−7.810	−7.8063±0.0026
	r	2.584	2.675	2.574	2.794±0.0014
	P	0.0393	0.0423	0.0334	
$pp\ ^3P_0$	a	−2.740	−2.876	−3.004	−4.82±1.11, −2.71±0.34
	r	3.867	3.831	3.312	7.14±0.93, 3.8±1.1
	P	−0.014	−0.0130	−0.0125	
$pp\ ^3P_1$	a	1.740	1.821	2.112	1.78±0.10, 1.97±0.09
	r	−8.196	−8.159	−8.269	−7.85±0.52, −8.27±0.37
	P	0.0009	0.0010	−0.0063	
$nn\ ^1S_0$	a	−23.76	−18.04	−18.05	−18.5±0.3, −18.9±0.4
	r	2.584	2.672	2.672	2.75±0.11
	P	0.0393	0.0423	0.0423	
$nn\ ^3P_0$	a	−2.740	−2.881	−2.881	
	r	3.867	3.823	3.822	
	P	−0.0140	−0.0131	−0.0131	
$nn\ ^3P_1$	a	1.740	1.823	1.823	
	r	−8.196	−8.151	−8.152	
	P	0.0009	0.0010	0.0010	
$np\ ^1S_0$	a	−23.76	−27.38	−27.87	−23.748±0.010
	r	2.584	2.528	2.525	2.75±0.05
	P	0.0393	0.0324	0.0324	
$np\ ^3P_0$	a	−2.740	−2.466	−2.466	
	r	3.867	3.929	3.929	
	P	−0.0140	−0.0186	−0.0186	
$np\ ^3S_1$	a	5.399	5.400	5.395	5.424±0.004
	r	1.730	1.730	1.730	1.759±0.005
	P	−0.010	−0.0096	−0.0097	
$np\ ^1P_1$	a	2.824	2.826	2.826	
	r	−6.294	−6.299	−6.299	
	P	−0.0058	−0.0058	−0.0058	
$np\ ^3P_1$	a	1.740	1.582	1.582	
	r	−8.196	−8.185	−8.185	
	P	0.0009	0.0004	0.0004	

results produced by the Paris potential [39] and the Bonn B potential [50] are also shown for comparison. The q_1 dependence of the nucleon s.p. potentials $U_N(q_1)$ obtained with the continuous choice is shown in Fig. 7 at three densities $\rho = 0.5\rho_0$, $0.7\rho_0$, and ρ_0, with $\rho_0 = 0.17$ fm^{-3} being the normal density. (These densities correspond to $k_F = 1.07$, 1.2, and 1.35 fm^{-1}, respectively.) For comparison, the results of the Nijmegen soft-core potential NSC89 [51] calculated by Schulze *et al.* [52] are also shown. The corresponding figure of $U_N(q_1)$ predicted by our previous model FSS is given in Fig. 2 of [6]. We find that fss2 gives the nucleon s.p. potential $U_N(q_1)$ very similar to that of FSS except for the higher momentum region $q_1 \geqslant 3$ fm^{-1}. As is discussed at the end of Sec. III A, the too attractive behavior of FSS in this momentum region is corrected in fss2, owing to the effect of the momentum-dependent Bryan-Scott terms involved in the

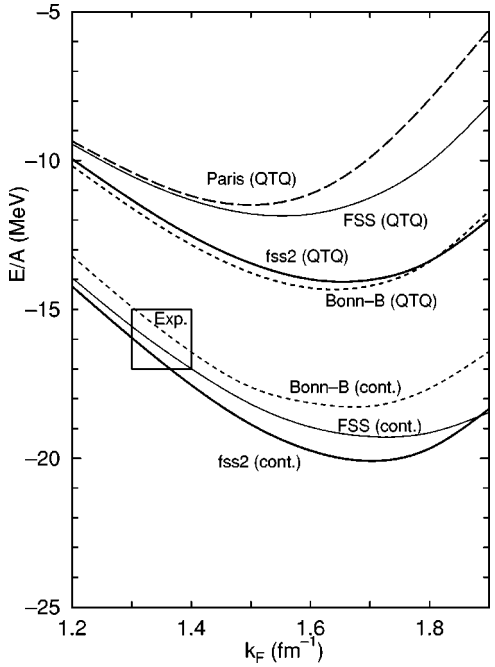

FIG. 6. Nuclear matter saturation curves obtained for fss2 and FSS, together with the results of the Paris potential [39] and the Bonn model-B (Bonn-B) potential [38]. The choice of the intermediate spectra is specified by "QTQ" and "cont.," respectively. The result for the Bonn-B potential in the continuous choice is taken from the nonrelativistic calculation in [50].

S-meson and V-meson exchange EMEP's. The saturation curve in Fig. 6 shows that this improvement of the s.p. potential in the high-momentum region has the favorable feature of moving the saturation density to the lower side, as long as the calculation is carried out with the continuous prescription. On the other hand, the saturation curve with the QTQ prescription suffers a rather large change in the transition from FSS to fss2. The prediction in fss2 with the QTQ prescription is very similar to the prediction in Bonn model-B potential. It is interesting to note that our fss2 result is rather close to Bonn model C for the deuteron properties (see Table V), while to model B for the nuclear saturation properties. The model B has a weaker tensor force than model C, which is a favorable feature for the nuclear saturation properties.

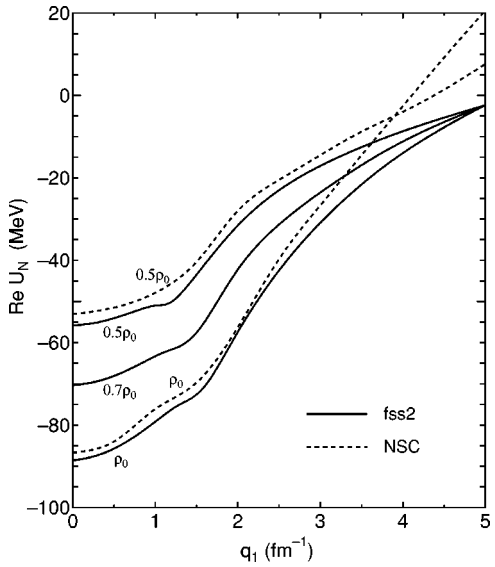

FIG. 7. The nucleon s.p. potential $U_N(q_1)$ in nuclear matter in the continuous choice for intermediate spectra. Predictions by fss2 for three densities $\rho=0.5\rho_0$, $0.7\rho_0$, and ρ_0 are shown. Here the normal density $\rho_0=0.17$ fm^{-3} corresponds to $k_F=1.35$ fm^{-1}. The dashed curves are the results achieved by Schulze *et al.* [52] with the Nijmegen soft-core NN potential NSC89 [51].

We should keep in mind that the short-range part of our quark model is mainly described by the quark-exchange mechanism. The nonlocal character of this part is entirely different from the usual V-meson-exchange picture in the standard meson-exchange models. In spite of this large difference the saturation point of our quark model does not deviate much from the Coester band, which indicates that our quark model has similar saturation properties with other realistic meson-exchange potentials.

By using the G-matrix solution of fss2, we can calculate the Sheerbaum factor S_B, which represents the strength of the s.p. spin-orbit potential defined through [25]

$$U_B^{ls}(\boldsymbol{r})=-\frac{\pi}{2}S_B\frac{1}{r}\frac{d\rho(r)}{dr}l\cdot\boldsymbol{\sigma}. \tag{3.2}$$

The explicit expression of $S_B(q_1)$ (which actually contains the momentum dependence) in terms of the G matrix is given in Eq. (50) of [25]. Here we only consider $S_B=S_B(q_1=0)$, as the measure of the s.p. spin-orbit strength in the bound states. The nucleon Sheerbaum factor obtained by fss2 is $S_N=-42.4$ MeV fm^5 at $k_F=1.35$ fm^{-1}, which is very close to the FSS value $S_N=-41.3$ MeV fm^5 [25]. However, the origin of the s.p. spin-orbit force is rather different between fss2 and FSS. In FSS the whole strength comes from the FB LS term, while in fss2 the S-meson EMEP yields appreciable contribution. This can be seen from the simple formula given in Eq. (52) of [25], which shows that in the Born approximation the FB LS contribution to the Scheerbaum factor is determined only by a single strength factor $\alpha_S x^3 m_{ud} c^2 b^5$. The value of this factor is 29.35 MeV fm^5 for fss2, which is 3/5 of the value of FSS, 48.91 MeV fm^5. This different origin of the s.p. spin-orbit force influences the Scheerbaum factor of the Λ hyperon, which will be discussed in a forthcoming paper.

IV. SUMMARY

The present-day strangeness nuclear physics is rapidly progressing in revealing very rich phenomena of the strong interaction both in the few-baryon systems and in various types of infinite nuclear matter. It is, therefore, very important to construct a realistic model of the baryon-baryon interaction, which can simultaneously reproduce all the available experimental data for the nucleon-nucleon (NN) and hyperon-nucleon (YN) interactions. The present framework, incorporating both the quark and mesonic degrees of freedom into the model space explicitly, is versatile enough to

predict more general baryon-baryon interactions for the complete baryon octet (B_8), since the color SU_3 and the spin-flavor SU_6 symmetries are exactly treated in the unambiguous framework of the resonating-group method. The model is based on the natural picture that the quarks and gluons are the most economical ingredients in the short-range region, while the meson-exchange processes are dominant in the medium- and long-range part of the interaction.

Since our quark model describes the short-range repulsion (which is observed in many channels of the baryon-baryon interactions) in terms of the nonlocality of the quark-exchange kernel, the effect of the short-range correlation is rather moderate, compared with the standard meson-exchange potentials. This can be seen in the magnitude of the Born amplitudes used in solving the Lippmann-Schwinger RGM (LS-RGM [7]) and the Bethe-Goldstone equations [6], and also in the fairly reasonable reproduction of the single-particle (s.p.) spin-orbit strengths calculated in the Born approximation [25]. In [7], we have seen that the Born amplitudes of the quark model have almost the same order of magnitude as the empirical scattering amplitudes obtained by solving the LS-RGM equation. The s.p. spin-orbit strength S_N predicted by the G-matrix solution of our quark model is almost equal to that in the Born approximation [25], in contrast to the standard potential models like the Reid soft-core potential with the strong short-range repulsive core [53]. Since the Born amplitudes in the quark model reflect rather faithfully the characteristic features of the LS-RGM solution, it is easy to find missing ingredients that impair the model.

In this study we upgrade our previous model FSS [3,4] in two respects. The first one is the renovation of the effective meson-exchange potentials (EMEPs) acting between quarks. We extend our model to include not only the leading terms of the scalar and pseudoscalar mesons but also the vector mesons with all possible standard terms usually used in the nonrelativistic one-boson-exchange potentials (OBEPs). The second point is the exact incorporation of the pion-Coulomb correction in the particle basis. This includes the exact treatment of the threshold energies and the Coulomb exchange kernel, as well as the separate evaluation of the spin-flavor factors of the charged- and neutral-pion exchange EMEP's. This improvement is necessary in order to study the effect of the charge symmetry breaking in the NN and YN interactions. These two renovations require various mathematical techniques which are specifically developed in Refs. [7] and [12] for these purposes. Appendix A in [7] discusses a convenient transformation formula of the RGM kernel, which directly gives the Born kernel for the momentum-dependent EMEPs at the quark level. A procedure to avoid the difficulties of threshold energies in the RGM formalism is given in [12]. The new model fss2 with these features has acquired much freedom to describe the NN and YN interactions more accurately than FSS. Three different types of calculations are carried out using fss2. The first one is the calculation in the isospin basis, which is used for determining the model parameters and also for the G-matrix calculation. The second and third calculations are done in the particle basis with and without the Coulomb force. When the Coulomb force is included, the standard technique by Vincent and Phatak [36] is employed to solve the LS-RGM equation in the momentum representation.

This paper discusses the NN system. The incorporation of the momentum-dependent Bryan-Scott term [8] and the vector-meson EMEPs improves the quantitative agreement to the experimental data to a large extent. The momentum-dependent Bryan-Scott term, included in the scalar- and vector-meson EMEPs, is favorable in extending our quark-model description of the NN scattering at the nonrelativistic energies to the higher energies up to $T_{\rm lab}=800$ MeV and also in describing reasonable asymptotic behavior of the s.p. potentials in the high-momentum region. For vector mesons, we avoid the criticism of the double counting [28] with the Fermi-Breit contribution by choosing small coupling constants around 1 especially for the flavor-singlet coupling constants $f_1^{\rm Ve}$ and $f_1^{\rm Vm}$. Since we have also chosen $f_8^{\rm Ve}=0$, the LS contribution from the vector mesons is almost negligible. For the ρ- and K^*-meson contributions, the selected value $f_8^{\rm Vm}\sim 2.6$ through the parameter search is a standard size usually assumed in OBEPs. Although the $(f_8^{\rm Vm})^2$ term usually gives the isovector spin-spin, tensor, and quadratic spin-orbit (QLS) terms, we only retain the QLS term with the $\boldsymbol{L}^2$-type spin-spin term. This choice at the quark level is rather *ad hoc*, but favorable since we do not want to introduce too strong cancellation between the one-pion tensor force and the ρ-meson tensor force in the ${}^3S_1$-${}^3D_1$ coupling term of the NN interaction. Since the $(3q)$ cluster wave function yields a large cutoff effect for the singular part of the one-pion-exchange potential, we introduce a reduction factor c_δ for the spin-spin contact term and multiply the short-range tensor term of the Fermi-Breit interaction by about factor 3. With these phenomenological ingredients, the accuracy of the model in the NN sector has now become almost comparable to that of the OBEP models. For the energies above the pion threshold, our single-channel calculation of the NN scattering seems to have given nearly satisfactory results, which are visible in the good reproduction of the differential cross sections up to $T_{\rm lab}=800$ MeV. The polarizations for the np and pp scattering have some unfavorable oscillations in the energy range $T_{\rm lab}=400$–800 MeV, but the improvement is a future work which definitely requires the explicit introduction of the inelastic channels such as the ΔN channel.

The G-matrix calculation using fss2 shows that our previous results given by FSS is qualitatively pertinent. In particular, the nucleon s.p. potentials in symmetric nuclear matter are very similar to the predictions of other realistic NN potentials. The nuclear saturation curve predicted by fss2 resembles the curve given by the Bonn model-B potential. It is interesting to note that the deuteron properties of fss2 are rather close to those of model C, which is known to have a larger D-state probability than model B. Since fss2 reproduces the NN phase shifts at nonrelativistic energies quite well, the difference of the off-shell effect between our quark model and the other OBEP models does not seem to appear so prominently, as far as the nuclear saturation curve is concerned.

In a forthcoming paper, we will discuss the YN interac-

TABLE VII. The spatial part of the exchange Born amplitudes defined by Eq. (A.4) of [7]. The polynomial part $\tilde{u}(\boldsymbol{k},\boldsymbol{q})$ of the two-body force in Eq. (A3) is also shown. The coefficients α, ϵ, $\Delta=2pq/(1-\tau^2)$, and the vectors $\boldsymbol{\rho}_{\mathcal{T}}=(\boldsymbol{V}/\sqrt{2\mu}b)$, $\boldsymbol{\sigma}_{\mathcal{T}}=(\boldsymbol{A}/\sqrt{2\mu}b)$ are calculated from Eq. (A14) of [7] by setting $x=1$ and $\mu=3/2$ for each interaction type $\mathcal{T}$. The factor Δ is nonzero only for the $\mathcal{T}=D_{\pm}$ types and $\epsilon\neq 0$ only for the $\mathcal{T}=S$, S' types. The basic spatial functions $f^{\Omega}_{\mathcal{T}}(\theta)$ with $\mathcal{T}=C$, CD, LS, TD are defined by Eq. (A10).

Ω	$\tilde{u}(\boldsymbol{k},\boldsymbol{q})$	$M^{\Omega}_{1\mathcal{T}}(\boldsymbol{q}_f,\boldsymbol{q}_i)$
C	1	$f^{C}_{\mathcal{T}}(\theta)$
SS	$\boldsymbol{k}^2$	$-m^2 f^{CD}_{\mathcal{T}}(\theta)$
$C(1)$	$\boldsymbol{q}^2$	$\frac{3}{4b^2}\left(1-\frac{\alpha}{2\mu}+\frac{1}{3}b^2\boldsymbol{\sigma}_{\mathcal{T}}^2\right)f^{C}_{\mathcal{T}}(\theta)-m^2\left(\frac{\epsilon}{4\mu}\right)^2 f^{CD}_{\mathcal{T}}(\theta)-m^2\frac{\epsilon}{4\mu}b^2(\boldsymbol{\rho}_{\mathcal{T}}\cdot\boldsymbol{\sigma}_{\mathcal{T}})f^{LS}_{\mathcal{T}}(\theta)$
$SS(1)$	$\boldsymbol{n}^2$	$-\frac{m^2}{2b^2}\left(1-\frac{\alpha}{2\mu}\right)f^{CD}_{\mathcal{T}}(\theta)+\frac{m^2}{2}\boldsymbol{\sigma}_{\mathcal{T}}^2 f^{LS}_{\mathcal{T}}(\theta)-\left(\frac{\Delta}{2\mu^2}\right)^2\boldsymbol{n}^2 f^{TD}_{\mathcal{T}}(\theta)$
T	$\mathcal{Y}_{2\mu}(\boldsymbol{k})$	$-f^{TD}_{\mathcal{T}}(\theta)\ \ \mathcal{Y}_{2\mu}(\boldsymbol{\rho}_{\mathcal{T}})$
QLS	$\mathcal{Y}_{2\mu}(\boldsymbol{n})$	$-\frac{m^2}{4}f^{LS}_{\mathcal{T}}(\theta)\ \ \mathcal{Y}_{2\mu}(\boldsymbol{\sigma}_{\mathcal{T}})+\frac{1}{4b^2}\left(1-\frac{\alpha}{2\mu}\right)f^{TD}_{\mathcal{T}}(\theta)\ \ \mathcal{Y}_{2\mu}(\boldsymbol{\rho}_{\mathcal{T}})-\left(\frac{\Delta}{2\mu^2}\right)^2 f^{TD}_{\mathcal{T}}(\theta)\ \ \mathcal{Y}_{2\mu}(\boldsymbol{n})$
LS	$i\boldsymbol{n}$	$\left(\frac{mb}{\mu}\right)^2\frac{\Delta}{2}f^{LS}_{\mathcal{T}}(\theta)i\boldsymbol{n}$

tion given by fss2. Further extension to more general B_8B_8 interactions with the strangeness $S=-2$, -3, and -4 will also be shown. Since all the model parameters are already determined in the $S=0$ and -1 sectors, these are all predictions which should be confronted with the future experimental data.

ACKNOWLEDGMENTS

This research is supported by Japan Grant-in-Aid for Scientific Research from the Ministry of Education, Science, Sports and Culture (12640265).

APPENDIX A: EMEP EXCHANGE KERNEL

In this appendix we extend the derivation of the EMEP exchange kernel developed in Appendixes A and B in [7], to deal with various interaction pieces of the V mesons, including the LS and QLS terms. The Coulomb exchange kernel and internal-energy contribution from EMEP are also discussed.

The systematic evaluation of the quark-exchange kernel is carried out by assuming a two-body interaction

$$U_{ij}=\sum_{\Omega}\ \alpha^{\Omega}w_{ij}^{\Omega'}\ \ u_{ij}^{\Omega''}, \tag{A1}$$

where $w_{ij}^{\Omega'}$ represents the spin-flavor part (the color part is $w_{ij}^{C}=1$ for EMEP's) and $u_{ij}^{\Omega''}$ the spatial part. Four different types of the spin-flavor factors $\Omega=C$, SS, T, LS are required for the most general EMEP's up to the V mesons: $w^{C}=1$, $w^{SS}=(\boldsymbol{\sigma}_1\cdot\boldsymbol{\sigma}_2)$, $w^{T}=[\sigma_1\sigma_2]^{(2)}_{\mu}$, and $w^{LS}=(\boldsymbol{\sigma}_1+\boldsymbol{\sigma}_2)/2$. For the flavor-octet mesons, these spin operators should be multiplied with $(\lambda_i\lambda_j)$, where λ represents the Gell-Mann matrix in the flavor SU_3 space. The spin-flavor factors $X^{\Omega}_{x\mathcal{T}}$ are defined by Eq. (A.3) of [7] for each w_{ij}^{Ω} with the quark-exchange number $x=0$, 1 and the five interaction types $\mathcal{T}=E$, S, S', D_+, D_- [54]. The noncentral factors are defined by the reduced matrix elements for the tensor operators of ranks 1 and 2. For example, the tensor operator is expressed as

$$\begin{aligned}S_{12}(\boldsymbol{k},\boldsymbol{k})&=3(\boldsymbol{\sigma}_1\cdot\boldsymbol{k})(\boldsymbol{\sigma}_2\cdot\boldsymbol{k})-(\boldsymbol{\sigma}_1\cdot\boldsymbol{\sigma}_2)\boldsymbol{k}^2\\&=3\sqrt{10}[[\sigma_1\sigma_2]^{(2)}\mathcal{Y}_2(\boldsymbol{k})]^{(0)},\end{aligned} \tag{A2}$$

where $\mathcal{Y}_{2\mu}(\boldsymbol{k})=\sqrt{4\pi/15}\boldsymbol{k}^2Y_{2\mu}(\hat{\boldsymbol{k}})$. The reduced matrix elements of the spin operators at the baryon level are assumed to be 1. For the spatial part, we also need three extra types $\Omega=C(1)$, $SS(1)$, QLS listed in Table VII. This table shows the polynomial functions $\tilde{u}(\boldsymbol{k},\boldsymbol{q})$ accompanied with the Yukawa function in the momentum representation through

$$u(\boldsymbol{k},\boldsymbol{q})=\frac{4\pi}{\boldsymbol{k}^2+m^2}\tilde{u}(\boldsymbol{k},\boldsymbol{q}) \tag{A3}$$

and the spatial part of the Born kernel $M^{\Omega}_{1\mathcal{T}}(\boldsymbol{q}_f,\boldsymbol{q}_i)$ defined in Eq. (A.4) of [7] explicitly. The formulas (A.18)–(A.21) given in [7] greatly simplify the procedure to obtain these results. The spatial functions $f^{\Omega}_{\mathcal{T}}(\theta)$ are explicitly given below.

In Eq. (A1) the coefficients α^{Ω} and the correspondence among Ω, Ω', and Ω'' are tabulated in Table VIII. The EMEP contribution of the exchange Born kernel in Eq. (2.4) is calculated through

$$M^{\Omega}(\boldsymbol{q}_f,\boldsymbol{q}_i)\mathcal{O}^{\Omega}(\boldsymbol{q}_f,\boldsymbol{q}_i)=\alpha^{\Omega}\sum_{\mathcal{T}}\ X^{\Omega'}_{1\mathcal{T}}\ \ M^{\Omega''}_{1\mathcal{T}}(\boldsymbol{q}_f,\boldsymbol{q}_i). \tag{A4}$$

The final result is as follows. For the central part, we have $\Omega=C$, $C(1)$, SS, $SS(1)$ types with

$$M^{C(\mathrm{S}_{\mathrm{V}})}(\boldsymbol{q}_f,\boldsymbol{q}_i)=\begin{pmatrix}-g^2\\ f_e^2\end{pmatrix}\sum_{\mathcal{T}} X^{C}_{1\mathcal{T}} f^{C}_{\mathcal{T}}(\theta),$$

$$M^{C(1)(\mathrm{S}_{\mathrm{V}})}(\boldsymbol{q}_f,\boldsymbol{q}_i)=2\gamma^2\begin{pmatrix}g^2\\ 3f_e^2\end{pmatrix}\sum_{\mathcal{T}} X^{C}_{1\mathcal{T}} f^{C(1)}_{\mathcal{T}}(\theta),$$

$$M^{SS(\mathrm{PS}_{\mathrm{V}})}(\boldsymbol{q}_f,\boldsymbol{q}_i)=\begin{pmatrix}f^2\dfrac{1}{3}\left(\dfrac{m}{m_{\pi^+}}\right)^2\\ f_m^2\dfrac{2}{3}\end{pmatrix}\sum_{\mathcal{T}} X^{SS}_{1\mathcal{T}} f^{CD}_{\mathcal{T}}(\theta),$$

$$M^{SS(1)(\mathrm{S}_{\mathrm{V}})}(\boldsymbol{q}_f,\boldsymbol{q}_i)=\begin{pmatrix}g^2\dfrac{1}{3}\gamma^4\\ -f_m^2\dfrac{8}{3}\gamma^2\end{pmatrix}\sum_{\mathcal{T}} X^{SS}_{1\mathcal{T}} f^{SS(1)}_{\mathcal{T}}(\theta). \tag{A5}$$

Here $\gamma=(m/2m_{ud})$. In these central terms, the spin-flavor factors $X^{C,SS}_{1E}$ should be replaced with $-X^{C,SS}_{1S'}$, because of the subtraction of the internal-energy contribution in the prior form. The tensor parts of the PS and V mesons are given by

$$M^{T(\mathrm{PS}_{\mathrm{V}})}(\boldsymbol{q}_f,\boldsymbol{q}_i)=\begin{pmatrix}f^2\left(\dfrac{m}{m_{\pi^+}}\right)^2\\ -f_m^2\end{pmatrix}\frac{1}{3m^2}{\sum_{\mathcal{T}\neq E}}' X^{T}_{1\mathcal{T}} f^{TD}_{\mathcal{T}}(\theta), \tag{A6}$$

where the V-meson contribution is also given for completeness although this term is not used in fss2. The EMEP QLS contribution reads

$$M^{QLS(\mathrm{S}_{\mathrm{V}})}(\boldsymbol{q}_f,\boldsymbol{q}_i)=\begin{pmatrix}g^2\dfrac{1}{3}\gamma^4\\ -f_m^2\dfrac{8}{3}\gamma^2\end{pmatrix}[X^{T}_{1D_+} f^{QLS}_{D_+}(\theta) - X^{T}_{1D_-} f^{QLS}_{D_-}(\theta)], \tag{A7}$$

but also contains the tensor contribution

$$M^{QT(\mathrm{S}_{\mathrm{V}})}(\boldsymbol{q}_f,\boldsymbol{q}_i)=\begin{pmatrix}g^2\dfrac{1}{3}\gamma^4\\ -f_m^2\dfrac{8}{3}\gamma^2\end{pmatrix}\frac{1}{4m^2}{\sum_{\mathcal{T}\neq E}}' X^{T}_{1\mathcal{T}} f^{QT}_{\mathcal{T}}(\theta), \tag{A8}$$

which we call $\Omega=QT$ term. In Eqs. (A7) and (A8), the QLS contribution from the S meson is also shown for completeness, although this term is negligibly small in fss2. The LS term has the contribution both from the S meson and the V meson:

$$M^{LS(\mathrm{S}_{\mathrm{V}})}(\boldsymbol{q}_f,\boldsymbol{q}_i)=-\begin{pmatrix}g^2(b\gamma)^2\\ -f_m f_e 4b^2\gamma\end{pmatrix}[X^{LS}_{1D_+} f^{LS}_{D_+}(\theta) - X^{LS}_{1D_-} f^{LS}_{D_-}(\theta)]. \tag{A9}$$

TABLE VIII. The coefficients α^{Ω} and the correspondence among Ω, Ω', Ω'' in the two-body force Eq. (A1). The column β implies the meson types and $\gamma=(m/2m_{ud})$ with m being the meson mass.

β	Ω	α^{Ω}	$w^{\Omega'}$	$u^{\Omega''}$
	C	$-g^2$	w^C	u^C
	$C(1)$	$g^2\dfrac{2\gamma^2}{m^2}$	w^C	$u^{C(1)}$
S	$SS(1)$	$g^2\dfrac{\gamma^4}{3m^4}$	w^{SS}	$u^{SS(1)}$
	QLS	$g^2\dfrac{\gamma^4}{3m^4}$	w^T	u^{QLS}
	LS	$-g^2\dfrac{2\gamma^2}{m^2}$	w^{LS}	u^{LS}
PS	SS	$-f^2\dfrac{1}{3m^2_{\pi^+}}$	w^{SS}	u^{SS}
	T	$-f^2\dfrac{1}{3m^2_{\pi^+}}$	w^T	u^T
	C	f_e^2	w^C	u^C
	$C(1)$	$f_e^2\dfrac{6\gamma^2}{m^2}$	w^C	$u^{C(1)}$
	SS	$-f_m^2\dfrac{2}{3m^2}$	w^{SS}	u^{SS}
V	$SS(1)$	$-f_m^2\dfrac{8\gamma^2}{3m^4}$	w^{SS}	$u^{SS(1)}$
	T	$f_m^2\dfrac{1}{3m^2}$	w^T	u^T
	QLS	$-f_m^2\dfrac{8\gamma^2}{3m^4}$	w^T	u^{QLS}
	LS	$-f_m f_e\dfrac{8\gamma}{m^2}$	w^{LS}	u^{LS}

For the tensor and QLS tensor terms in Eqs. (A6) and (A8), each interaction term with $\mathcal{T}=S$, S', D_+, D_- types should be rearranged to $\Omega=T$, T', T'' types in Eq. (2.6), according to the rules given in Eq. (B.13) or (B.17) of [7].

The EMEP spatial functions $f^{\Omega}_{\mathcal{T}}(\theta)$ used here are defined by extending $f^{CN}_{\mathcal{T}}(\theta)$, $f^{SN}_{\mathcal{T}}(\theta)$, and $f^{TN}_{\mathcal{T}}(\theta)$ given in Eq. (B.18) of [7]. The following four basic functions are used in Table VII:[5]

[5]Note that $f^{C}_{\mathcal{T}}(\theta)=-f^{CN}_{\mathcal{T}}(\theta)$ and $f^{CD}_{\mathcal{T}}(\theta)=3f^{SN}_{\mathcal{T}}(\theta)$ except for the difference of c_δ, but $f^{TD}_{\mathcal{T}}(\theta)$ here contains different numerical factors from those of $f^{TN}_{\mathcal{T}}(\theta)$.

$$f_{\mathcal{T}}^{C}(\theta)=4\pi\left(\frac{3}{2}\right)^{3/2}\hbar c b^2\begin{cases}\exp\left\{-\frac{1}{3}b^2(\boldsymbol{q}^2+\boldsymbol{k}^2)\right\}\tilde{\mathcal{Y}}_{\alpha_E}(0)\\ \left(\frac{8}{11}\right)^{1/2}\exp\left\{-\frac{2}{11}b^2\left[\frac{4}{3}(\boldsymbol{q}^2+\boldsymbol{k}^2)-\boldsymbol{k}\cdot\boldsymbol{q}\right]\right\}\tilde{\mathcal{Y}}_{\alpha_S}\left(\frac{1}{\sqrt{11}}b|\boldsymbol{q}+\boldsymbol{k}|\right)\\ \left(\frac{1}{2}\right)^{1/2}\exp\left\{-\frac{1}{3}b^2\left(\boldsymbol{q}^2+\frac{1}{4}\boldsymbol{k}^2\right)\right\}\tilde{\mathcal{Y}}_{\alpha_{D_+}}\left(\frac{1}{2}b|\boldsymbol{k}|\right)\\ \left(\frac{2}{3}\right)^{1/2}\exp\left\{-\frac{1}{3}b^2\boldsymbol{k}^2\right\}\tilde{\mathcal{Y}}_{\alpha_{D_-}}\left(\frac{1}{\sqrt{3}}b|\boldsymbol{q}|\right)\end{cases}\quad\text{for}\quad\mathcal{T}=\begin{cases}E,\\ S,\\ D_+,\\ D_-,\end{cases}$$

$$f_{\mathcal{T}}^{CD}(\theta)=f_{\mathcal{T}}^{C}(\theta)\ \text{ with }\ \tilde{\mathcal{Y}}_{\alpha_{\mathcal{T}}}(\rho)\to\tilde{\mathcal{Y}}_{\alpha_{\mathcal{T}}}(\rho)-\frac{1}{2\alpha_{\mathcal{T}}},$$

$$f_{\mathcal{T}}^{LS}(\theta)=f_{\mathcal{T}}^{C}(\theta)\ \text{ with }\ \tilde{\mathcal{Y}}_{\alpha_{\mathcal{T}}}(\rho)\to\tilde{\mathcal{Z}}_{\alpha_{\mathcal{T}}}^{(1)}(\rho),$$

$$f_{\mathcal{T}}^{TD}(\theta)=-4\pi\left(\frac{3}{2}\right)^{3/2}\hbar c b^2\begin{cases}\left(\frac{8}{11}\right)^{5/2}\exp\left\{-\frac{2}{11}b^2\left[\frac{4}{3}(\boldsymbol{q}^2+\boldsymbol{k}^2)-\boldsymbol{k}\cdot\boldsymbol{q}\right]\right\}\tilde{\mathcal{Z}}_{\alpha_S}^{D}\left(\frac{1}{\sqrt{11}}b|\boldsymbol{q}+\boldsymbol{k}|\right)\\ \left(\frac{1}{2}\right)^{5/2}\exp\left\{-\frac{1}{3}b^2\left(\boldsymbol{q}^2+\frac{1}{4}\boldsymbol{k}^2\right)\right\}\tilde{\mathcal{Z}}_{\alpha_{D_+}}^{D}\left(\frac{1}{2}b|\boldsymbol{k}|\right)\\ \left(\frac{2}{3}\right)^{5/2}\exp\left\{-\frac{1}{3}b^2\boldsymbol{k}^2\right\}\tilde{\mathcal{Z}}_{\alpha_{D_-}}^{D}\left(\frac{1}{\sqrt{3}}b|\boldsymbol{q}|\right)\end{cases}\quad\text{for}\quad\mathcal{T}=\begin{cases}S,\\ D_+,\\ D_-.\end{cases}\tag{A10}$$

The S'-type spatial function $f_{S'}^{\Omega}(\theta)$ is obtained from $f_{S}^{\Omega}(\theta)$ by taking $\boldsymbol{k}\to-\boldsymbol{k}$. There is no E-type possible for the noncentral terms. The coefficients $\alpha_{\mathcal{T}}$ are given by $\alpha_S=\alpha_{S'}=(11/8)\alpha_E$, $\alpha_{D_+}=2\alpha_E$, and $\alpha_{D_-}=(3/2)\alpha_E$, with $\alpha_E=(mb)^2/2=(1/2)\times(mcb/\hbar)^2$. For the spin-spin part of the one-pion-exchange EMEP, $\tilde{\mathcal{Y}}_{\alpha_{\mathcal{T}}}(\rho)-(1/2\alpha_{\mathcal{T}})$ should be modified into $\tilde{\mathcal{Y}}_{\alpha_{\mathcal{T}}}(\rho)-c_\delta\ (1/2\alpha_{\mathcal{T}})$. The modified Yukawa functions $\tilde{\mathcal{Y}}_\alpha(\rho)$, $\tilde{\mathcal{Z}}_\alpha^{(1)}(\rho)$, and $\tilde{\mathcal{Z}}_\alpha(\rho)$ are essentially given by the error function of the imaginary argument:

$$\tilde{\mathcal{Y}}_\alpha(\rho)=e^{\alpha-\rho^2}\int_0^1 e^{-\alpha/t^2+\rho^2t^2}dt,\quad \tilde{\mathcal{Z}}_\alpha^{(1)}(\rho)=\frac{1}{2\alpha}e^{\alpha-\rho^2}\int_0^1 e^{-\alpha/t^2+\rho^2t^2}t^2dt,\quad \tilde{\mathcal{Z}}_\alpha^{D}(\rho)=e^{\alpha-\rho^2}\int_0^1 e^{-\alpha/t^2+\rho^2t^2}t^4dt.\tag{A11}$$

The other spatial functions appearing in Eqs. (A5)–(A9) are defined by using the four spatial functions in Eq. (A10):

$$f_{\mathcal{T}}^{C(1)}(\theta)=\left[\frac{3}{8\alpha_E}\begin{Bmatrix}1\\ \frac{5}{8}\\ \frac{1}{2}\\ 0\end{Bmatrix}+\left(\frac{1}{2m}\right)^2\begin{Bmatrix}0\\ \frac{1}{4}(\boldsymbol{k}+\boldsymbol{q})^2\\ \boldsymbol{q}^2\\ \boldsymbol{k}^2\end{Bmatrix}\right]f_{\mathcal{T}}^{C}(\theta)-\left(\frac{3}{16}\right)^2\begin{Bmatrix}0\\ 1\\ 0\\ 0\end{Bmatrix}f_{\mathcal{T}}^{CD}(\theta)-\frac{3}{16}b^2\begin{Bmatrix}0\\ \frac{1}{4}(\boldsymbol{k}+\boldsymbol{q})^2\\ 0\\ 0\end{Bmatrix}f_{\mathcal{T}}^{LS}(\theta)$$

$$\text{for}\quad\mathcal{T}=\begin{cases}E,\\ S,\\ D_+,\\ D_-,\end{cases}$$

$$f_{\mathcal{T}}^{SS(1)}(\theta)=-\frac{1}{4\alpha_E}\begin{Bmatrix}1\\ \frac{5}{8}\\ \frac{1}{2}\\ 0\end{Bmatrix}f_{\mathcal{T}}^{CD}(\theta)-\left(\frac{1}{2m^2}\right)^2\begin{Bmatrix}0\\ 0\\ 1\\ 1\end{Bmatrix}\boldsymbol{n}^2f_{\mathcal{T}}^{TD}(\theta)+\frac{1}{2m^2}\begin{Bmatrix}0\\ \frac{1}{4}(\boldsymbol{k}+\boldsymbol{q})^2\\ \boldsymbol{q}^2\\ \boldsymbol{k}^2\end{Bmatrix}f_{\mathcal{T}}^{LS}(\theta)\quad\text{for}\quad\mathcal{T}=\begin{cases}E,\\ S,\\ D_+,\\ D_-,\end{cases}$$

$$f^{QLS}_{D_\pm}(\theta)=-\frac{1}{4}\left(\frac{1}{m}\right)^4 f^{TD}_{D_\pm}(\theta),$$

$$f^{QT}_{\mathcal{T}}(\theta)=\begin{cases}\dfrac{1}{2\alpha_E}\dfrac{5}{8}f^{TD}_S(\theta)-f^{LS}_S(\theta)\\ \dfrac{1}{2\alpha_E}\dfrac{1}{2}f^{TD}_{D_+}(\theta)-f^{LS}_{D_-}(\theta)\\ -f^{LS}_{D_+}(\theta)\end{cases}\quad\text{for}\quad\mathcal{T}=\begin{cases}S,\\ D_+,\\ D_-.\end{cases}\tag{A12}$$

For the numerical calculation, it is convenient to include the direct term also in the above expressions. This can be achieved in Eqs. (A5)–(A9), if we further add $X^{\Omega'}_{0D_+}f^{\Omega''}_D(\theta)$ term, in addition to the $X^{\Omega'}_{1D_+}f^{\Omega''}_{1D_+}(\theta)$ term. The direct-type spatial functions $f^{\Omega}_D(\theta)$ are given by

$$f^C_D(\theta)=\frac{4\pi}{\boldsymbol{k}^2+m^2}e^{-(m\boldsymbol{k})^2/3}\tag{A13}$$

and

$$f^{\Omega}_D(\theta)=f^C_D(\theta)\begin{cases}-\dfrac{\boldsymbol{k}^2}{m^2}\\ -1\\ \dfrac{1}{3\alpha_E}\\ \left(\dfrac{1}{m}\right)^2\left(\dfrac{1}{9}\boldsymbol{q}^2+\dfrac{1}{2b^2}\right)\\ \left(\dfrac{1}{m}\right)^4\left(\dfrac{1}{9}\boldsymbol{n}^2+\dfrac{1}{3b^2}\boldsymbol{k}^2\right)\\ \dfrac{1}{9}\left(\dfrac{1}{m}\right)^4\\ -\dfrac{1}{3\alpha_E}\end{cases}\quad\text{for}\quad\Omega=\begin{cases}CD,\\ TD,\\ LS,\\ C(1),\\ SS(1),\\ QLS,\\ QT.\end{cases}\tag{A14}$$

The Coulomb exchange kernel is very similar to the color-Coulombic term of the FB interaction, as is discussed in Sec. II D. Only difference is (1) $\alpha_S\to\alpha=(e^2/\hbar c)$, (2) the definition of the Coulomb spin-flavor factor

$$X^{CL}_{x\mathcal{T}}=C_x\left\langle z_x\xi\left|\sum_{i<j}^{\mathcal{T}}Q_iQ_j\right|\xi\right\rangle,\tag{A15}$$

and (3) the modification of the spatial function $\tilde{h}_0(\rho)$ in Eq. (B.5) of [7], by the effect of the Coulomb cutoff at R_C. The last modification is achieved by

$$\tilde{h}_0(\rho)\to\tilde{h}_0(\rho)-g(x,\rho),$$

$$g(x,\rho)=e^{-(\rho^2+x^2)}\int_0^1 e^{\rho^2t^2}\cos(2\rho xt)dt,\tag{A16}$$

with $x=(1/\sqrt{2})(R_C/b)$, $(2/\sqrt{11})(R_C/b)$, $(1/2)(R_C/b)$, and $(1/\sqrt{3})(R_C/b)$ for the $\mathcal{T}=E$, S or S', D_+, and D_- types, respectively. The function $g(x,\rho)$ is expressed as

$$\begin{aligned}g(x,\rho)&=\frac{\sqrt{\pi}}{2\rho}e^{-\rho^2}\ \mathrm{Im}\,\mathrm{erf}(x+i\rho)\\ &=\frac{\sqrt{\pi}}{2\rho}e^{-x^2}[\sin(2\rho x)\mathrm{Re}\,w(\rho+ix)\\ &\quad+\cos(2\rho x)\mathrm{Im}\,w(\rho+ix)],\end{aligned}\tag{A17}$$

where $w(z)=e^{-z^2}\mathrm{erfc}(-iz)$ with $\mathrm{erfc}(z)=1-\mathrm{erf}(z)$. We note the simple relationship

$$g(0,\rho)=\frac{\sqrt{\pi}}{2\rho}\mathrm{Im}\,w(\rho)=\tilde{h}_0(\rho),$$

$$g(x,0)=e^{-x^2}.\tag{A18}$$

For example, the $\mathcal{T}=E$ type spatial function is given by $f^{CL}_E(\theta)=\sqrt{2/\pi}\alpha x m_{ud}c^2(4/3)f(\theta)(1-e^{-(R_C/b)^2/2})$, since $\tilde{h}_0(0)=1$ [cf. Eq. (2.18)].

The EMEP contribution to the internal energies of the octet baryons originates only from the central force. It reads

$$\begin{aligned}E^{\mathrm{S}}_{\mathrm{int}}&=mg^2X^C_{0E}\left[\left(-1+\frac{3\gamma^2}{4\alpha_E}\right)Y_{\alpha_E}(0)+\frac{\gamma^2}{2}Y^D_{\alpha_E}(0)\right]\\ &\quad-mg^2X^{SS}_{0E}\frac{\gamma^4}{12\alpha_E}Y^D_{\alpha_E}(0),\\ E^{\mathrm{PS}}_{\mathrm{int}}&=\frac{m}{3}f^2\left(\frac{m}{m_{\pi^+}}\right)^2X^{SS}_{0E}Y^D_{\alpha_E}(0),\\ E^{\mathrm{V}}_{\mathrm{int}}&=mf_e^2X^C_{0E}\left[\left(1+\frac{9\gamma^2}{4\alpha_E}\right)Y_{\alpha_E}(0)+\frac{\gamma^2}{2}Y^D_{\alpha_E}(0)\right]\\ &\quad+mf_m^2X^{SS}_{0E}\frac{2}{3}\left(1+\frac{\gamma^2}{\alpha_E}\right)Y^D_{\alpha_E}(0),\end{aligned}\tag{A19}$$

where the values of the modified Yukawa functions at the origin are given by $Y_\alpha(0)=1/\sqrt{\pi\alpha}-e^\alpha\mathrm{erfc}(\sqrt{\alpha})$ and $Y^D_\alpha(0)=Y_\alpha(0)-1/(2\alpha\sqrt{\pi\alpha})$. The $\gamma^2|2Y^D_{\alpha_E}(0)$ contributions in Eq. (A19), which correspond to the $\mathbf{k}^{2/4}$ momentum-dependent Bryan-Scott term, are neglected in the present calculation (see Sec. II. C).

APPENDIX B: DEUTERON WAVE FUNCTIONS

The relative wave functions for the deuteron in the momentum representation, $f_l(q)\sim 1/(\gamma^2+q^2)T_{l,-}(q,-i\gamma,-\epsilon_d)$, satisfy the homogeneous equation

$$\begin{aligned}(\gamma^2+p^2)f_l(p)&=-\frac{2\mu}{\hbar^2}\frac{4\pi}{(2\pi)^3}\sum_{l'}\int_0^\infty q^2dq\\ &\quad\times V_{ll'}(p,q,-\epsilon_d)f_{l'}(q),\end{aligned}\tag{B1}$$

where $V_{ll'}(p,q,-\epsilon_d)$ is the partial-wave components of Eq. (2.8). Since $f_l(q)$ are the relative wave functions of the

TABLE IX. The coefficients C_j and D_j in Eq. (B6) for the parametrized deuteron wave functions. The model is fss2, calculated in the particle basis with the full Coulomb exchange kernel. The number of parameters is $n=11$, but the last C_j and the last three D_j (the parenthesized values) should be calculated from Eqs. (C.7) and (C.8) of [38].

j	γ_j	C_j (fm$^{-1/2}$)	D_j (fm$^{-1/2}$)
1	0.23186542	0.88177292969	$0.22317366018\times10^{-1}$
2	1.13186542	-0.22759285797	-0.47989721024
3	2.03186542	$-0.87378082999\times10^{-1}$	0.70358390560
4	2.93186542	$-0.19214145234\times10^{2}$	$-0.19602848976\times10^{2}$
5	3.83186542	$0.19019661123\times10^{3}$	$0.16245688580\times10^{3}$
6	4.73186542	$-0.10079545619\times10^{4}$	$-0.75342203360\times10^{3}$
7	5.63186542	$0.28344069046\times10^{4}$	$0.19989675989\times10^{4}$
8	6.53186542	$-0.44819643416\times10^{4}$	$-0.30666624647\times10^{4}$
9	7.43186542	$0.40462956321\times10^{4}$	$(0.27047041824\times10^{4})$
10	8.33186542	$-0.19571100406\times10^{4}$	$(-0.12779605335\times10^{4})$
11	9.23186542	$(0.39477713946\times10^{3})$	$(0.25127320956\times10^{3})$

RGM equation, one needs to renormalize them through the square root of the normalization kernel [4]. This can be achieved by calculating

$$F_l(q)=qf_l(q)+q\sum_N R_{Nl}(q,b^2/3)\frac{\gamma_N}{\sqrt{1+\gamma_N}+1}J_{Nl}, \tag{B2}$$

where $R_{Nl}(r,\nu)$ represents the radial part of the harmonic-oscillator wave function with the width parameter ν, and $\gamma_N=(1/3)^{N+2}$ with $N=0, 2, 4, \ldots$ are the eigenvalues of the exchange normalization kernel for the ^3E states of the NN system. The harmonic-oscillator components J_{Nl} of $f_l(q)$ are calculated from

$$J_{Nl}=\int_0^\infty q^2dqR_{Nl}(q,b^2/3)f_l(q). \tag{B3}$$

The deuteron wave functions $u_l(r)$ in the coordinate representation [customarily written as $u(r)=u_0(r)$ and $w(r)=u_2(r)$ for the S-wave and D-wave states, respectively] are obtained from the Fourier transformation

$$u_l(r)=i^l\sqrt{\frac{2}{\pi}}\int_0^\infty dq(qr)j_l(qr)F_l(q). \tag{B4}$$

In particular, $f_l(q)$ are normalized such that

$$\sum_l\int_0^\infty dr[u_l(r)]^2=\sum_l\int_0^\infty dq[F_l(q)]^2=1. \tag{B5}$$

We follow the standard ansatz [55,38,9] for the simple parametrization of the deuteron wave functions:

$$F_l(q)=\sum_{j=1}^n\begin{Bmatrix}C_j\\D_J\end{Bmatrix}\sqrt{\frac{2}{\pi}}\frac{q}{q^2+\gamma_j^2}\quad\text{for}\quad\begin{cases}l=0,\\l=2,\end{cases}$$

$$u_l(r)=\begin{cases}\displaystyle\sum_{j=1}^n C_je^{-\gamma_jr}\\ \displaystyle\sum_{j=1}^n D_je^{-\gamma_jr}\left(1+\frac{3}{\gamma_jr}+\frac{3}{(\gamma_jr)^2}\right)\end{cases}\quad\text{for}\quad\begin{cases}l=0,\\l=2.\end{cases} \tag{B6}$$

The range parameters γ_j are chosen as $\gamma_j=\gamma+(j-1)\gamma_0$ with $\gamma_0=0.9$ fm^{-1} and $n=11$. The coefficients C_j ($j=1$–10) and D_j ($j=1$–8) with $\gamma=0.231\,865\,42$ fm^{-1} are given in Table IX for the deuteron wave functions in the full calculation. The other coefficients, namely, the last C_j and the last three D_j, should be calculated from Eqs. (C.7) and (C.8) of [38].

[1] Y. Fujiwara, C. Nakamoto, and Y. Suzuki, Prog. Theor. Phys. **94**, 215 (1995).
[2] Y. Fujiwara, C. Nakamoto, and Y. Suzuki, Prog. Theor. Phys. **94**, 353 (1995).
[3] Y. Fujiwara, C. Nakamoto, and Y. Suzuki, Phys. Rev. Lett. **76**, 2242 (1996).
[4] Y. Fujiwara, C. Nakamoto, and Y. Suzuki, Phys. Rev. C **54**, 2180 (1996).
[5] T. Fujita, Y. Fujiwara, C. Nakamoto, and Y. Suzuki, Prog. Theor. Phys. **100**, 931 (1998).
[6] M. Kohno, Y. Fujiwara, T. Fujita, C. Nakamoto, and Y. Suzuki, Nucl. Phys. **A674**, 229 (2000).
[7] Y. Fujiwara, M. Kohno, T. Fujita, C. Nakamoto, and Y. Suzuki, Prog. Theor. Phys. **103**, 755 (2000).
[8] R. A. Bryan and B. L. Scott, Phys. Rev. **164**, 1215 (1967).
[9] R. Machleidt, Phys. Rev. C **63**, 024001 (2001).
[10] M. Jurič *et al.*, Nucl. Phys. **B52**, 1 (1973).
[11] M. M. Nagels, T. A. Rijken, and J. J. de Swart, Ann. Phys. (N.Y.) **79**, 338 (1973).
[12] Y. Fujiwara, M. Kohno, C. Nakamoto, and Y. Suzuki, Prog.

Theor. Phys. **104**, 1025 (2000).
[13] Scattering Analysis Interactive Dial-up (SAID), Virginia Polytechnic Institute, Blacksburg, Virginia, R. A. Arndt (private communication).
[14] *Quark Cluster Model of Baryon-Baryon Interactions*, edited by M. Oka, K. Shimizu, and K. Yazaki [Prog. Theor. Phys. Suppl. **137**, 1 (2000)].
[15] F. Fernández, A. Valcarce, U. Straub, and A. Faessler, J. Phys. G **19**, 2013 (1993).
[16] A. Valcarce, A. Buchmann, F. Fernández, and Amand Faessler, Phys. Rev. C **50**, 2246 (1994); **51**, 1480 (1995).
[17] Zong-ye Zhang, Amand Faessler, U. Straub, and L. Ya. Glozman, Nucl. Phys. **A578**, 573 (1994).
[18] L. J. Qi, J. H. Zhang, P. N. Shen, Z. Y. Zhang, and Y. W. Yu, Nucl. Phys. **A585**, 693 (1995).
[19] Y. W. Yu, Z. Y. Zhang, P. N. Shen, and L. R. Dai, Phys. Rev. C **52**, 3393 (1995).
[20] D. R. Entem, F. Fernández, and A. Valcarce, Phys. Rev. C **62**, 034002 (2000).
[21] S. Yang, P. N. Shen, Z. Y. Zhang, and Y. W. Yu, Nucl. Phys. **A635**, 146 (1998).
[22] C. Nakamoto, Y. Suzuki, and Y. Fujiwara, Prog. Theor. Phys. **94**, 65 (1995).
[23] H. P. Noyes, Phys. Rev. Lett. **15**, 538 (1965).
[24] K. L. Kowalski, Phys. Rev. Lett. **15**, 798, 908(E) (1965).
[25] Y. Fujiwara, M. Kohno, T. Fujita, C. Nakamoto, and Y. Suzuki, Nucl. Phys. **A674**, 493 (2000).
[26] Y. Fujiwara, Prog. Theor. Phys. **88**, 933 (1992).
[27] Y. Fujiwara, C. Nakamoto, Y. Suzuki, and Zhang Zong-ye, Prog. Theor. Phys. **97**, 587 (1997).
[28] K. Yazaki, Prog. Part. Nucl. Phys. **24**, 353 (1990).
[29] T. Hamada and I. D. Johnston, Nucl. Phys. **34**, 382 (1962).
[30] V. G. J. Stoks, R. A. M. Klomp, C. P. F. Terheggen, and J. J. de Swart, Phys. Rev. C **49**, 2950 (1994).
[31] K. Miyagawa and H. Yamamura, Phys. Rev. C **60**, 024003 (1999).
[32] S. Shinmura, Y. Akaishi, and H. Tanaka, Prog. Theor. Phys. **71**, 546 (1983).
[33] Y. Yamamoto, T. Motoba, H. Himeno, K. Ikeda, and S. Nagata, Prog. Theor. Phys. Suppl. **117**, 361 (1994).
[34] E. Hiyama, Nucl. Phys. **A670**, 273c (2000).
[35] H. Nemura, Y. Suzuki, Y. Fujiwara, and C. Nakamoto, Prog. Theor. Phys. **103**, 929 (2000).
[36] C. M. Vincent and S. C. Phatak, Phys. Rev. C **10**, 391 (1974).
[37] V. G. J. Stoks, R. A. M. Klomp, M. C. M. Rentmeester, and J. J. de Swart, Phys. Rev. C **48**, 792 (1993).
[38] R. Machleidt, Adv. Nucl. Phys. **19**, 189 (1989).
[39] M. Lacombe, B. Loiseau, J. M. Richard, R. Vinh Mau, J. Côté, P. Pirès, and R. de Tourreil, Phys. Rev. C **21**, 861 (1980).
[40] O. Dumbrajs, R. Koch, H. Pilkuhn, G. C. Oades, H. Behrens, J. J. de Swart, and P. Kroll, Nucl. Phys. **B216**, 277 (1983).
[41] L. J. Allen, H. Fiedeldey, and N. J. McGurk, J. Phys. G **4**, 353 (1978).
[42] M. Kohno, J. Phys. G **9**, L85 (1983).
[43] N. L. Rodning and L. D. Knutson, Phys. Rev. C **41**, 898 (1990).
[44] David M. Bishop and Lap M. Cheung, Phys. Rev. A **20**, 381 (1979).
[45] G. A. Miller, M. K. Nefkens, and I. Slaus, Phys. Rep. **194**, 1 (1990).
[46] C. R. Howell *et al.*, Phys. Lett. B **444**, 252 (1998).
[47] D. E. González Trotter *et al.*, Phys. Rev. Lett. **83**, 3788 (1999).
[48] J. R. Bergervoet, P. C. van Campen, W. A. van der Sanden, and J. J. de Swart, Phys. Rev. C **38**, 15 (1988).
[49] M. M. Nagels, T. A. Rijken, and J. J. de Swart, Phys. Rev. D **12**, 744 (1975).
[50] R. Brockmann and R. Machleidt, Phys. Rev. C **42**, 1965 (1990).
[51] P. M. M. Maessen, Th. A. Rijken, and J. J. de Swart, Phys. Rev. C **40**, 2226 (1989).
[52] H.-J. Schulze, M. Baldo, U. Lombardo, J. Cugnon, and A. Lejeune, Phys. Rev. C **57**, 704 (1998).
[53] R. R. Scheerbaum, Nucl. Phys. **A257**, 77 (1976).
[54] Y. Fujiwara and Y. C. Tang, Memoirs of the Faculty of Science, Kyoto University, Series A of Physics, Astrophysics, Geophysics and Chemistry, 1994, Vol. XXXIX, No. 1, Article 5, p. 91.
[55] M. Lacombe, B. Loiseau, J. Richard, R. Vinh Mau, J. Côté, P. Pirès, and R. de Tourreil, Phys. Lett. **101B**, 139 (1981).